

# A numerical procedure to study the stability of helical vortices

Yonghui Xu<sup>1,2</sup>, Ivan Delbende<sup>1\*</sup>, Yuji Hattori<sup>3</sup>, Maurice Rossi<sup>1</sup>

<sup>1\*</sup>Sorbonne Université, CNRS, UMR 7190, Institut Jean le Rond d'Alembert, 75005 Paris, France.

<sup>2</sup>present address: Research Center for Aircraft Systems Engineering Technology, Qianwan Institute of CNITECH, Ningbo 315336, China.

<sup>3</sup>Institute of Fluid Science, Tohoku University, Sendai 980-8577, Japan.

\*Corresponding author(s). E-mail(s): [ivan.delbende@sorbonne-universite.fr](mailto:ivan.delbende@sorbonne-universite.fr);  
Contributing authors: [xuyonghui@nimte.ac.cn](mailto:xuyonghui@nimte.ac.cn); [yuji.hattori@tohoku.ac.jp](mailto:yuji.hattori@tohoku.ac.jp);  
[maurice.rossi@sorbonne-universite.fr](mailto:maurice.rossi@sorbonne-universite.fr);

## Abstract

A numerical approach is proposed for the study of instabilities in helical vortex systems as found in the near-wake of turbines or propellers. The methodology has a high degree of generality, yet the present paper focusses on the case of one unique helical vortex. First, a method based on helical symmetry aimed at computing a three-dimensional base flow with prescribed parameters – helical pitch, helical radius, vortex circulation, core size and inner jet component — is presented. Second, the linear instability of this base flow is examined by reducing the three-dimensional instability problem to two-dimensional simulations with wavenumbers prescribed along the helix axis. Each simulation converges towards an exponentially growing or decaying complex state from which eigenfunctions, growth rate and frequency are extracted. This procedure is validated against a standard method based on direct three-dimensional numerical simulations of the Navier–Stokes equations linearized in the vicinity of the same helical base flows. Three illustrative base flows are presented with or without inner jet component, the instability of which is dominated, at the prescribed axial wavenumber, by unstable modes of three different types: long-wave instability, short-wave elliptic and curvature instabilities. Results from the new procedure and from the fully three-dimensional one are found in excellent agreement, which validates the new methodology. The gain in computational time is typically the one that is achieved while going from three-dimensional to two-dimensional simulations.

**Keywords:** vortex dynamics, helical vortex, instability, elliptic instability, curvature instability, numerical simulation

# 1 Introduction

Wind energy is one of the fastest growing source of renewable energy. Hence a better understanding of the aerodynamics of wind turbine systems and of the wake dynamics can help us improve the efficiency of energy extraction. The structure generated at the tip of a turbine blade is a helical vortex. In the near wake of a  $N$ -blade rotor, a well-organized structure is observed:  $N$  nearly identical helical vortices, each of circulation  $\Gamma$  as well as a central hub vortex of circulation  $-N\Gamma$ . The hub vortex is centered along the wind-turbine axis while the  $N$  tip vortices of radius  $R$  are regularly spaced along the azimuth about the wind turbine axis ( $R$  being close to the blade length). Experimentally, each vortex found in the wake of a rotor system is also characterized by its core size and by an internal jet/wake component. This latter feature might be important since, for *straight* vortices, an internal jet component is known to strongly modify the Kelvin waves [1] and to change the stability properties *via* the swirling jet instability [2, 3]. Similar consequences may be present for helical vortices.

Such a system of helical vortices and hub vortex evolves at downstream distance into a turbulent flow [4]. We are interested here in the near-range wake, which plays an important role in the transition. Numerous theoretical studies have been conducted on the stability of helical vortices. Both long-wave and short-wave instability modes were found. Short-wave modes take their origin from the resonance or near resonance between two Kelvin waves propagating along the vortex core. This resonance is mediated by a deformation of the base flow due to an external strain field, the curvature or the torsion of the vortex and may result in unstable perturbations, namely elliptic or curvature instability modes [5–7]. Such instabilities have already been documented for vortex rings [8]. Long-wave modes involve the displacement of vortices while their core structure remains untouched. Their dynamics have been mainly predicted in the framework of vortex filaments [9–11]. Helical vortex instabilities were also experimentally studied [12]. Some quite recent results give evidence to the long-wave mode [13–16].

Three-dimensional (3D) direct numerical simulations (DNS) have been used to study the dynamics of such vortex systems [17]. Abraham *et al.* [18] simulated an asymmetric rotor to trigger such long-wave instability and thus indirectly enhance turbulent mixing and wake recovery. However, the details of the transition to turbulence in such systems have not been described so far. Using DNS for such a task would be much time consuming and results may be difficult to analyze. A different approach is proposed here in which the evolution in the near-wake is studied in terms of instability theory. A two-step procedure is performed: first, we define a base state which is simple enough so that its stability analysis is tractable and second, we study the dynamics of general infinitesimal perturbations in the vicinity of this base flow. This latter could be an equilibrium state, that is a fixed point of the governing equations, or else an exact steady solution of the Navier–Stokes equations. If one excepts spatially uniform and solid-body rotation flows, an unbounded viscous flow without external forcing never remains steady, as its kinetic energy is converted into thermal energy by viscosity. Nevertheless, it is standard to use the stability theory upon a base solution which is steady for the Euler equations, but unsteady for the Navier–Stokes equations. In such an instance, for high Reynolds number, this base flow — if sufficiently smooth — slowly changes over time by viscous diffusion. This flow is called a quasi-equilibrium

state. From experimental observations, it seems appropriate for the wake behind a propeller to search for a base flow which possesses a *helical symmetry* of *helix pitch*  $2\pi L$  along a given axis. This means that we are looking for a base flow invariant with respect to a rotation of any angle  $\Delta\theta$  around the  $z$ -axis coupled with a translation of  $\Delta z = L\Delta\theta$  along the same axis [19]. Mathematically, a scalar field  $G$  such as the pressure field depends only on two variables  $r$  and  $\theta - z/L$ , namely  $G = G(r, \theta - z/L, t)$  and the velocity field is such that

$$\mathbf{u} = u_r(r, \theta - z/L, t)\mathbf{e}_r(\theta) + u_\theta(r, \theta - z/L, t)\mathbf{e}_\theta(\theta) + u_z(r, \theta - z/L, t)\mathbf{e}_z. \quad (1)$$

This flow uniformly rotates around the  $z$ -axis so it may be made steady in a rotating frame or in a translating frame along the  $z$ -axis. For a wind turbine, each helical vortex possesses an approximate wavelength  $2\pi L$  along the turbine axis (the  $z$ -axis) so that, in the Betz regime, the reduced pitch  $L/R$  is typically of order 0.1 when the tip-speed ratio is of order 10 [20].

In the present paper, our purpose is not to describe the stability of wind turbine wakes that will be the focus of future works, but to explain in an accurate manner the numerical tool that we developed to perform such an analysis. A first procedure aims at computing a quasi-equilibrium state which is helically symmetric, with prescribed values for circulation, radial position, core size of vortices as well as their inner jet intensity. This is not straightforward and needs to employ an iterative approach. Thereafter, the paper addresses the stability of this three-dimensional flow and describes a method to compute the instability modes. Such problem has already been considered by Brynjell-Rahkola & Henningson [21]. These authors solve a 3D Poisson equation to build up a helical state with prescribed vorticity that they inject as an initial condition into a 3D Navier–Stokes solver to obtain a quasi-equilibrium state. Thereafter, they extract the dominant instability modes using a matrix-free method linked to an implicitly restarted Arnoldi algorithm in the full 3D context. They were able to identify long- and short-wave elliptic instabilities on a two-helical vortex system. In such methodology, an integer number of instability wavelengths is necessarily present in the axially periodic computational box (see section 5 for discussion). We herein present a two-dimensional (2D) alternative to their fully 3D method, that is *a priori* faster and is not subject to this limitation in wavenumber. We validate our numerical approach by presenting cases of long- and short-wave modes. The results are compared to a linearized three-dimensional method using the same baseflow, in the simplest configuration of one helical vortex (one blade without hub vortex).

The structure of the paper is as follows: in section 2, the three-dimensional Navier–Stokes equations are written using helical variables. The methodology used to characterize a helical vortex and to obtain a helical base flow with prescribed characteristics are described in section 3; examples of base flows without or with inner jet component along the helical vortex core are provided in §3.5. Section 4 describes the way instability modes are computed using helical variables, while section 5 presents how the instability study is performed with fully three-dimensional simulations. Results and comparisons between both methods are given in section 6 for so-called long- and short-wave instability modes. Conclusions are given in section 7.

## 2 The Navier–Stokes equations written with helical variables

We assume the fluid to be incompressible and viscous. As a consequence, the dynamics is governed by the Navier–Stokes equations. In velocity–pressure formulation, it is written as

$$\begin{aligned} \frac{\partial \mathbf{u}}{\partial t} + \boldsymbol{\omega} \times \mathbf{u} &= -\nabla G + \nu \Delta \mathbf{u} \\ \nabla \cdot \mathbf{u} &= 0, \end{aligned} \quad (2)$$

where  $\mathbf{u}$  stands for velocity and  $\boldsymbol{\omega}$  for vorticity. Parameter  $\nu$  is the kinematic viscosity while the scalar field  $G$  represents the total head

$$G \equiv \frac{p}{\rho_{\text{fl}}} + \frac{1}{2} \mathbf{u}^2, \quad (3)$$

with  $\rho_{\text{fl}}$  the fluid density and  $p$  the pressure field. Let us change variables from the standard cylindrical coordinates  $(r, \theta, z)$  to helical coordinates  $(\bar{r}, \bar{\varphi}, \bar{z})$ :

$$\bar{r} = r, \quad \bar{\varphi} \equiv \theta - z/L, \quad \bar{z} = z, \quad (4)$$

while still using the cylindrical coordinate basis  $(\mathbf{e}_r, \mathbf{e}_\theta, \mathbf{e}_z)$ . The first and second derivatives with respect to the cylindrical coordinates in system (2) can be expressed with the helical coordinates using the relations ( $p$  is a positive integer):

$$\begin{aligned} \frac{\partial^p}{\partial r^p} &= \frac{\partial^p}{\partial \bar{r}^p}, \quad \frac{\partial^p}{\partial \theta^p} = \frac{\partial^p}{\partial \bar{\varphi}^p}, \quad \frac{\partial}{\partial z} = \frac{\partial}{\partial \bar{z}} - \frac{1}{L} \frac{\partial}{\partial \bar{\varphi}}, \\ \frac{\partial^2}{\partial z^2} &= \frac{\partial^2}{\partial \bar{z}^2} - \frac{2}{L} \frac{\partial^2}{\partial \bar{z} \partial \bar{\varphi}} + \frac{1}{L^2} \frac{\partial^2}{\partial \bar{\varphi}^2}. \end{aligned} \quad (5)$$

The expression of operators in these equations changes accordingly. *From now on, we only use coordinates  $(\bar{r}, \bar{\varphi}, \bar{z})$  for operator derivatives and remove the overbar.* However we still use the azimuth  $\theta$  of the global cylindrical coordinate system. The divergence  $\nabla \cdot \mathbf{u}$  of velocity vector  $\mathbf{u}$  then reads:

$$\nabla \cdot \mathbf{u} = \frac{1}{r} \frac{\partial(r u_r)}{\partial r} + \frac{1}{r} \frac{\partial u_\theta}{\partial \varphi} + \frac{\partial u_z}{\partial z} - \frac{1}{L} \frac{\partial u_z}{\partial \varphi}. \quad (6)$$

Similarly, the gradient  $\nabla G$  of the total head becomes

$$\nabla G = \frac{\partial G}{\partial r} \mathbf{e}_r + \frac{1}{r} \frac{\partial G}{\partial \varphi} \mathbf{e}_\theta + \left( \frac{\partial G}{\partial z} - \frac{1}{L} \frac{\partial G}{\partial \varphi} \right) \mathbf{e}_z. \quad (7)$$

The three components of the Laplacian of velocity field  $\Delta \mathbf{u}$  take the following form:

$$\begin{aligned}
(\Delta \mathbf{u})_r &= \frac{\partial}{\partial r} \left( \frac{1}{r} \frac{\partial(r u_r)}{\partial r} \right) + \frac{1}{r^2} \frac{\partial^2 u_r}{\partial \varphi^2} + \frac{\partial^2 u_r}{\partial z^2} - \frac{2}{L} \frac{\partial^2 u_r}{\partial z \partial \varphi} + \frac{1}{L^2} \frac{\partial^2 u_r}{\partial \varphi^2} - \frac{2}{r^2} \frac{\partial u_\theta}{\partial \varphi} \\
(\Delta \mathbf{u})_\theta &= \frac{\partial}{\partial r} \left( \frac{1}{r} \frac{\partial(r u_\theta)}{\partial r} \right) + \frac{1}{r^2} \frac{\partial^2 u_\theta}{\partial \varphi^2} + \frac{\partial^2 u_\theta}{\partial z^2} - \frac{2}{L} \frac{\partial^2 u_\theta}{\partial z \partial \varphi} + \frac{1}{L^2} \frac{\partial^2 u_\theta}{\partial \varphi^2} + \frac{2}{r^2} \frac{\partial u_r}{\partial \varphi} \\
(\Delta \mathbf{u})_z &= \frac{1}{r} \frac{\partial}{\partial r} \left( r \frac{\partial u_z}{\partial r} \right) + \frac{1}{r^2} \frac{\partial^2 u_z}{\partial \varphi^2} + \frac{\partial^2 u_z}{\partial z^2} - \frac{2}{L} \frac{\partial^2 u_z}{\partial z \partial \varphi} + \frac{1}{L^2} \frac{\partial^2 u_z}{\partial \varphi^2}.
\end{aligned} \tag{8}$$

This latter formula for  $(\Delta \mathbf{u})_z$  also defines the Laplacian  $\Delta G$  of a *scalar* field  $G(r, \varphi, z)$  in helical coordinates. By taking the curl of velocity, one computes the vorticity components

$$\begin{aligned}
\omega_r &= \frac{1}{r} \frac{\partial u_z}{\partial \varphi} + \frac{1}{L} \frac{\partial u_\theta}{\partial \varphi} - \frac{\partial u_\theta}{\partial z} \\
\omega_\theta &= \frac{\partial u_r}{\partial z} - \frac{1}{L} \frac{\partial u_r}{\partial \varphi} - \frac{\partial u_z}{\partial r} \\
\omega_z &= \frac{1}{r} \frac{\partial}{\partial r} (r u_\theta) - \frac{1}{r} \frac{\partial u_r}{\partial \varphi},
\end{aligned} \tag{9}$$

and thereafter the components of the product  $\boldsymbol{\omega} \times \mathbf{u}$ .

### 3 Building a helically symmetric quasi-equilibrium base flow

In this section, we propose a method to build a base state representing a system of helical vortices generally characterized by a total circulation  $\Gamma_{\text{tot}}$ , an external velocity  $U_z^\infty$  at  $r \rightarrow \infty$  and which is periodic along the  $z$ -axis of period  $2\pi L$ . This system could be made of  $N$  identical helical vortices each characterized by a circulation  $\Gamma$  and a central hub of circulation  $-N\Gamma$  so that  $\Gamma_{\text{tot}} = 0$  or it could be the same system without hub so that  $\Gamma_{\text{tot}} = N\Gamma$ . Such helical vortices may contain some swirl i.e. an inner jet component along the vortex core, which makes right-handed and left-handed helices different. We present and test this method only on a single vortex but the other cases ( $N$  helical vortices with or without hub) can be treated in the same way with little and obvious modifications. We also set the fluid velocity at infinity to be zero  $U_z^\infty = 0$ . In an experimental or real flow, as for instance in the wake of a rotating device, this would amount to adopt the reference frame linked to the incoming flow.

For the study of stability of a single straight vortex, the base states are axisymmetric smooth solutions such as the Batchelor vortex profiles [22]. Indeed these clearly are Euler equilibria and hence quasi-equilibria of the Navier–Stokes equations. For a base flow with two straight vortices like a dipole, no quasi-equilibrium is known analytically. A quasi-equilibrium flow however can be rapidly reached starting from two axisymmetric profiles and running a purely two-dimensional simulation in which three-dimensional instability waves are filtered out. In this final state, each single vortex profile is no more axisymmetric with respect to its own axis but it is made slightly

elliptic because of the strain applied by one vortex on its companion. For helical vortices, no analytical Euler solutions are known. In the above spirit, we run a simulation in which helical symmetry is enforced (the HELIX flow solver) so that the non-helical unstable waves are filtered out. In general, a helical solution is not a quasi-equilibrium because self-induced strain is present. Nevertheless, in accordance with Ref. [23], we expect to reach such a quasi-equilibrium rapidly by running the HELIX solver from an initial state close to quasi-equilibrium. The HELIX solver is explained in §3.1, the initial condition is given in §3.2. How to check and characterize a quasi-equilibrium is explained in §3.3. The iterative algorithm allowing to reach a specific state with prescribed parameter values is presented §3.4.

### 3.1 Helically symmetric simulation

A helically symmetric flow is governed by the Navier–Stokes equations written in helical variables (see section 2) in which we set  $\partial_z = 0$ . This is a generalization of two-dimensional Navier–Stokes equations with three velocity components but it actually differs from the pure two-dimensional model, since here in-plane and normal components are coupled. In this section, we summarize the presentation to be found in Ref. [24], [19] and [23].

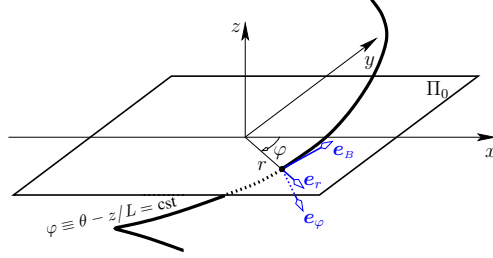


**Fig. 1** Geometry of a helical line.

Let us introduce the orthonormal Beltrami basis  $(\mathbf{e}_r, \mathbf{e}_\varphi, \mathbf{e}_B)$  (see figure 1):  $\mathbf{e}_B \equiv \alpha(\mathbf{e}_z + r\mathbf{e}_\theta/L)$  is directed along the tangent of helical lines  $(r, \varphi) = cst$  with  $\alpha(r) \equiv (1 + r^2/L^2)^{-1/2}$  and  $\mathbf{e}_\varphi = \mathbf{e}_B \times \mathbf{e}_r$ . In such a basis, a helically symmetric velocity field may be expressed as

$$\mathbf{u}(r, \varphi, t) = u_r(r, \varphi, t)\mathbf{e}_r(\theta) + u_\varphi(r, \varphi, t)\mathbf{e}_\varphi(r, \theta) + u_B(r, \varphi, t)\mathbf{e}_B(r, \theta), \quad (10)$$

with

$$u_\varphi = \alpha(u_\theta - ru_z/L), \quad u_B = \alpha(u_z + ru_\theta/L). \quad (11)$$

Similar expressions apply to the vorticity field  $\boldsymbol{\omega}$ . Incompressibility imposes

$$\nabla \cdot \mathbf{u} = \frac{1}{r} \frac{\partial (ru_r)}{\partial r} + \frac{1}{r\alpha} \frac{\partial u_\varphi}{\partial \varphi} = 0, \quad (12)$$

hence a stream function  $\Psi$  exists such that

$$ru_r = \partial_\varphi \Psi, \quad u_\varphi = -\alpha(r)\partial_r \Psi. \quad (13)$$

As a consequence, only the helical velocity  $u_B$  and the stream function  $\Psi$  are necessary to describe a helically symmetric velocity field:

$$\mathbf{u}(r, \varphi, t) = u_B \mathbf{e}_B + \alpha \nabla \Psi \times \mathbf{e}_B. \quad (14)$$

Introducing  $u_H \equiv u_B/\alpha - C_\infty$  where  $C_\infty \equiv \Gamma_{\text{tot}}/(2\pi L) + U_z^\infty$  and taking the curl of (14) yields

$$\omega_r = \frac{1}{r} \frac{\partial u_H}{\partial \varphi}, \quad \omega_\varphi = -\alpha \frac{\partial u_H}{\partial r}, \quad (15)$$

$$\omega_B = -\mathbb{L}\Psi + \frac{2\alpha^3}{L}(u_H + C_\infty), \quad \text{with } \mathbb{L}(\bullet) \equiv \frac{1}{r\alpha} \partial_r [r\alpha^2 \partial_r(\bullet)] + \frac{1}{r^2\alpha} \partial_{\varphi\varphi}(\bullet). \quad (16)$$

Since vorticity is localized in a bounded region of the  $(r, \varphi)$  plane, it is worth to use velocity  $u_H$  instead of  $u_B$ . Indeed velocity  $u_H$  must vanish away from vortices:  $u_H$  is bound to be constant away from the vorticity region, and this constant is zero by construction since  $u_B/\alpha \rightarrow C_\infty$  as  $r \rightarrow \infty$ .

Once we know  $\omega_B$  and  $u_H$ , we can compute the streamfunction  $\Psi$  by solving the Poisson equation (16) and therefore all the remaining velocity components are available. The time evolution depends on two dynamical equations: one for velocity  $u_H$  and one for vorticity  $\omega_B$ . The first one is obtained as follows. One rewrites the Navier–Stokes equation (2) introducing the vectorial relation  $\nabla^2 \mathbf{u} = -\nabla \times \boldsymbol{\omega}$ :

$$\frac{\partial}{\partial t} \mathbf{u} + \boldsymbol{\omega} \times \mathbf{u} = -\nabla G - \nu \nabla \times \boldsymbol{\omega}. \quad (17)$$

The above equation is then projected along the direction  $\mathbf{e}_B$  and divided by  $\alpha$  yielding an equation for  $u_H$ :

$$\partial_t u_H + \text{NL}_{u_H} = \nu \text{VT}_{u_H}, \quad (18)$$

where the viscous term and the nonlinear term take the form

$$\text{VT}_{u_H} \equiv \frac{1}{\alpha} \mathbb{L}u_H - \frac{2}{L} \alpha \omega_B, \quad \text{NL}_{u_H} = J(u_H, \Psi) \quad (19)$$

with

$$J(f, g) \equiv \frac{1}{r} (\partial_r f \partial_\varphi g - \partial_\varphi f \partial_r g).$$

The dynamical equation for vorticity  $\omega_B$  is obtained first by taking the curl of equation (17)

$$\frac{\partial}{\partial t} \boldsymbol{\omega} + \nabla \times (\boldsymbol{\omega} \times \mathbf{u}) = -\nu \nabla \times (\nabla \times \boldsymbol{\omega}) \quad (20)$$

and second by projecting this equation along  $\mathbf{e}_B$ . This yields

$$\partial_t \omega_B + \text{NL}_\omega = \nu \text{VT}_\omega, \quad (21)$$

where the viscous term and the nonlinear term take the form

$$\begin{aligned} \text{VT}_\omega &= \mathbb{L}\left(\frac{\omega_B}{\alpha}\right) - \left(\frac{2\alpha^2}{L}\right)^2 \omega_B + \frac{2\alpha^2}{L} \mathbb{L}(u_H), \\ \text{NL}_\omega &= \frac{1}{\alpha} J(\alpha\omega_B, \Psi) + \frac{2\alpha^3}{L} J(u_H, \Psi) + \frac{\alpha^3}{L^2} \partial_\varphi [(u_H + C_\infty)^2]. \end{aligned} \quad (22)$$

Quantities are  $2\pi$ -periodic along the  $\varphi$  direction and can be expanded using a Fourier decomposition:

$$\begin{pmatrix} \omega_B(r, \varphi, t) \\ u_H(r, \varphi, t) \\ \psi(r, \varphi, t) \end{pmatrix} = \sum_{n=-\infty}^{+\infty} \begin{pmatrix} \hat{\omega}_B^{(n)}(r, t) \\ \hat{u}_H^{(n)}(r, t) \\ \hat{\psi}^{(n)}(r, t) \end{pmatrix} \exp(in\varphi) \quad (23)$$

where mode  $(-n)$  is the complex conjugate of mode  $n$ .

For each  $n \geq 0$ , we first perform the time advance of equations deduced from (18) and (21) for  $\hat{\omega}_B^{(n)}(r, t)$  and  $\hat{u}_H^{(n)}(r, t)$ . Thereafter, we determine  $\hat{\psi}^{(n)}$  for  $n > 0$  by solving the following equation derived from (16):

$$\frac{1}{r\alpha} \partial_r (r\alpha^2 \partial_r \hat{\psi}^{(n)}) - \frac{n^2}{r^2\alpha} \hat{\psi}^{(n)} = -\hat{\omega}_B^{(n)} + \frac{2\alpha^3}{L} \hat{u}_H^{(n)}. \quad (24)$$

For  $n = 0$ , we only need  $\hat{u}_\varphi^{(0)}$  which is obtained by solving

$$\frac{1}{r\alpha} \partial_r (r\alpha \hat{u}_\varphi^{(0)}) = \hat{\omega}_B^{(0)} - \frac{2\alpha^3}{L} (\hat{u}_H^{(0)} + C_\infty). \quad (25)$$

Simulations are performed using a pseudo-spectral method in a finite domain  $r \leq R_{\text{ext}}$ . Details on the HELIX flow solver can be found in Ref. [19, 23, 24]. Conditions at  $r = R_{\text{ext}}$  have been improved with respect to these latter references and can be found in Appendix A.

### 3.2 Initial condition

The initial condition is chosen so that one reaches a quasi-equilibrium solution made of a single helical vortex of circulation  $\Gamma$  and helical pitch  $L$ . The pitch is directly prescribed by the helical solver HELIX and circulation is imposed by the initial condition since it is known to be a constant of motion. As mentioned in the introduction of section 3, this initial state is built not far from a quasi-equilibrium. We assume the initial flow to be a vortex filament located around a helix going through a point A located in the  $\Pi_0$  plane at cylindrical coordinates  $(r_A, \theta_A)$  and we define the plane  $\Pi_\perp$  as the plane containing point A and perpendicular to the helical line passing through this point (see figure 2a). Point A is associated with the Serret–Frenet basis  $(\mathbf{e}_\xi, \mathbf{e}_\eta, \mathbf{e}_b)$

$$\mathbf{e}_\xi = \mathbf{e}_r(\theta_A), \quad \mathbf{e}_\eta = \alpha_A \left[ \mathbf{e}_\theta(\theta_A) - \frac{r_A}{L} \mathbf{e}_z \right], \quad \mathbf{e}_b = \mathbf{e}_B(r_A, \theta_A) = \alpha_A \left[ \frac{r_A}{L} \mathbf{e}_\theta(\theta_A) + \mathbf{e}_z \right], \quad (26)$$

with  $\alpha_A \equiv (1 + r_A^2/L^2)^{-1/2}$ . The plane  $\Pi_\perp$  is thus orthogonal to unit vector  $\mathbf{e}_b$  and spanned by the Cartesian basis  $(\mathbf{e}_\xi, \mathbf{e}_\eta)$ . Point  $M_\perp \in \Pi_\perp$  can be located by the local polar coordinates  $(\rho, \psi)$  based on point A and the local polar basis  $(\mathbf{e}_\rho, \mathbf{e}_\psi)$  defined by

$$\mathbf{e}_\rho = \cos \psi \mathbf{e}_\xi + \sin \psi \mathbf{e}_\eta, \quad \mathbf{e}_\psi = -\sin \psi \mathbf{e}_\xi + \cos \psi \mathbf{e}_\eta. \quad (27)$$

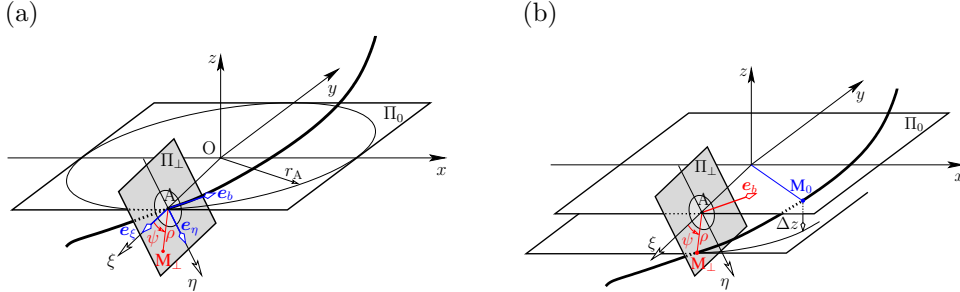


**Fig. 2** (a) Geometry of the helical vortex. (b) Illustration of the projection process from plane  $\Pi_\perp$  onto plane  $\Pi_0$  along helical lines, relating  $M_\perp$  to  $M_0$ .

The velocity profiles are axisymmetric and similar to the Batchelor vortex in the plane  $\Pi_\perp$ :

$$\omega_B(\rho) = \omega_B^* \exp\left(-\frac{\rho^2}{a_*^2}\right), \quad u_H(\rho) = u_H^* \exp\left(-\frac{\rho^2}{a_*^2}\right). \quad (28)$$

The amplitude  $\omega_B^*$  is determined by the circulation  $\Gamma$  and  $u_H^*$  [24]. If the core size  $a_*$  is small compared to  $r_A$  and  $L$ , it is locally approaching a quasi-equilibrium of two-dimensional flow with three components. In the HELIX solver, initial conditions are given in a plane  $\Pi_\perp$  associated to some point A (see section 3.4), it is thus necessary to transfer the data from plane  $\Pi_\perp$  to plane  $\Pi_0$  before starting the temporal integration. This procedure is explained in Appendix C.

### 3.3 Characterization of the final velocity state

At the end of a simulation, we check that the computed state is a quasi-equilibrium in a frame rotating with an angular velocity  $\Omega_0 \mathbf{e}_z$  about the  $z$  axis, where quantity  $\Omega_0$  is computed using the best correlation of the vorticity field between successive time steps. For this state, the specific conditions on  $\omega_B$ ,  $u_H$  and  $\Psi$  for quasi-equilibria [23] were found to be verified.

Apart from circulation  $\Gamma$  and pitch  $L$  which are fixed by the simulation, the helically symmetric vortex at a final time of simulation is characterized by a vortex center in plane  $\Pi_0$ . Its location at  $(R_f, \theta_f)$  corresponds to the point at which  $\Psi$  reaches a maximum in the vorticity region of plane  $\Pi_0$ , or equivalently for a quasi-equilibrium state (see discussion in [23]) the point at which  $u_H$  reaches an extremum (or  $\alpha\omega_B$  if  $u_H = 0$ ). For characterization, we need the field values of quasi-equilibrium state on the plane  $\Pi_\perp$  containing the vortex center and normal to this helical line, i.e.

normal to vector  $\mathbf{e}_b \equiv \mathbf{e}_B(R_f, \theta_f)$  for given sets of  $(\rho, \psi)$  values centered at point A on  $\Pi_\perp$  (see figure 2a). From relations (C22), we get  $(r_0, \varphi_0)$ . The field quantities  $u_r(r_0, \varphi_0)$ ,  $u_\varphi(r_0, \varphi_0)$  and  $u_B(r_0, \varphi_0)$  are then interpolated using the fields obtained by the simulation. This leads to  $u_\rho(\rho, \psi)$ ,  $u_\psi(\rho, \psi)$  and  $u_b(\rho, \psi)$ . The same procedure is applied for vorticity. The vortex core size  $a_f$  and inner jet parameter  $W_f$  are then computed by determining the axisymmetric parts  $\hat{\omega}_b^{(0)}$  and  $\hat{u}_b^{(0)}$  of  $\omega_b$  and  $u_b$ . The value  $a_f$  is obtained by a best fit of  $\hat{\omega}_b^{(0)}$  by the Gaussian expression:

$$\hat{\omega}_b^{(0)}(\rho) \approx \frac{\Gamma}{\pi a_f^2} \exp\left(-\frac{\rho^2}{a_f^2}\right). \quad (29)$$

Thereafter, the inner jet velocity  $W_f$  is determined by a best fit of  $\hat{u}_b^{(0)}$  by expression

$$\hat{u}_b^{(0)}(\rho) \approx W_f \exp\left(-\frac{\rho^2}{a_f^2}\right) + W_{ff}. \quad (30)$$

### 3.4 Iterative algorithm to obtain the prescribed base flow

Our purpose is to construct a base flow characterized by prescribed circulation  $\Gamma$ , reduced pitch  $L$ , helical radius  $R_0$ , core size  $a_0$  and inner jet parameter  $W_0$ , using the evaluation described in section 3.3. In the following, all variables are put in dimensionless form using  $R_0$  as a length scale and  $R_0^2/\Gamma$  as a time scale. As a consequence, the value  $\Gamma$  and  $R_0$  below are understood to be both equal to one. We define the Reynolds number as  $Re \equiv \Gamma/\nu$  where  $\nu$  stands for the kinematic viscosity.

The procedure is an iterative algorithm based at each iteration on a simulation of the Navier–Stokes equations starting from an initial condition based on the circulation  $\Gamma$  and pitch  $L$  as well as three guessed values of dimensionless parameters  $(R_\star, a_\star, u_H^\star)$ . The temporal integration is performed in two stages: an approach stage at low Reynolds number  $Re_1$  during a time period  $T_1$  followed by a second stage at the final Reynolds number  $Re_2 = Re$  during a time period  $T_2$ . The goal of the first stage is to rapidly dampen out Kelvin waves excited by the initial condition and to save computational time. The state then rapidly converges towards a quasi-equilibrium as shown in Ref. [23]. The state at the end of the simulation characterized by a radius  $R_f$ , core size  $a_f$  and inner jet parameter  $W_f$ . This defines three functions linking the initial parameters to the final ones:  $R_\star = F_R(R_f, a_f, W_f)$ ,  $a_\star^2 = F_{a^2}(R_f, a_f, W_f)$ ,  $u_H^\star = F_W(R_f, a_f, W_f)$ .

Based on numerical evidence [19], the helical radius and the square of the core size grow almost linearly in time

$$\frac{dr_A}{dt} \approx \frac{\lambda(L)}{Re}, \quad \frac{da^2}{dt} \approx \frac{4}{Re}. \quad (31)$$

As a consequence, functions  $F_R$ ,  $F_{a^2}$  may be well approximated by

$$F_R^{\text{appr}} = R_f - \lambda(L) \left( \frac{T_1}{Re_1} + \frac{T_2}{Re_2} \right), \quad F_{a^2}^{\text{appr}} = a_f^2 - 4 \left( \frac{T_1}{Re_1} + \frac{T_2}{Re_2} \right). \quad (32)$$

The relation (23) in Ref. [19]

$$\frac{d}{dt} \iint_{\Pi_0} u_H dS = -\frac{2\Gamma}{LRe} \quad (33)$$

together with the second formula (31) impose quantity

$$Q \equiv \iint_{\Pi_0} u_H dS + \frac{\Gamma}{2L} a^2 \quad (34)$$

to be time-invariant. Its expression at  $t = 0$  uses equation (28) and assumes  $a_\star$  to be small yielding

$$Q = \left( \frac{u_H^\star}{\alpha_\star} + \frac{\Gamma}{2\pi L} \right) a_\star^2 \quad \text{with } \alpha_\star \equiv \frac{1}{\sqrt{1 + (R_\star)^2/L^2}}. \quad (35)$$

The expression for  $Q$  at  $t = T_1 + T_2$  uses equation (30) and assumes  $a_f$  to be small

$$Q = \left( \frac{u_H^f}{\alpha_f} + \frac{\Gamma}{2\pi L} \right) a_f^2 \quad \text{with } \alpha_f \equiv \frac{1}{\sqrt{1 + (R_f)^2/L^2}}. \quad (36)$$

The relation found in Ref. [23]

$$u_H^f = \frac{W_f}{\alpha_f} - \frac{\Gamma \alpha_f}{2\pi L}, \quad (37)$$

yields

$$Q = \frac{W_f}{\alpha_f^2} a_f^2. \quad (38)$$

Comparing both expressions makes possible an approximation of  $F_W$ :

$$F_W^{\text{appr}} = \alpha_\star \left( \frac{a_f^2}{a_\star^2} \frac{W_f}{\alpha_f^2} - \frac{\Gamma}{2\pi L} \right). \quad (39)$$

For the first iteration (the first run), the guessed value for  $(R_\star, a_\star, u_H^\star)$  is based on the above approximation

$$R_\star = F_R^{\text{appr}}(R_0, a_0, W_0), \quad a_\star^2 = F_{a^2}^{\text{appr}}(R_0, a_0, W_0), \quad u_H^\star = F_W^{\text{appr}}(R_0, a_0, W_0). \quad (40)$$

Once the time-integration has been performed (at the end of each run), we check the condition

$$\max \left( \frac{|\epsilon_r|}{R_0}, \frac{|\epsilon_{a^2}|}{a_0^2}, |\epsilon_W| \right) < 10^{-3}, \quad (41)$$

where  $\epsilon_r \equiv R_f - R_0$ ,  $\epsilon_{a^2} \equiv a_f^2 - a_0^2$  and  $\epsilon_W \equiv W_f - W_0$ . If it is met, the values for parameters  $(R_\star, a_\star, u_H^\star)$  are considered as correct and the procedure stops. If not, the

three parameters are incremented. The correct increments  $\delta R_\star = F_R(R_0, a_0, W_0) - F_R(R_f, a_f, W_f)$ ,  $\delta a_\star^2 = F_{a^2}(R_0, a_0, W_0) - F_{a^2}(R_f, a_f, W_f)$  and  $\delta u_{H\star}^\star = F_W(R_0, a_0, W_0) - F_W(R_f, a_f, W_f)$  are then approximated by linearizing around  $(R_0, a_0, W_0)$  and approximating the derivatives of functions  $F_R$ ,  $F_{a^2}$  and  $F_W$  at  $(R_0, a_0, W_0)$  by the derivatives of  $F_R^{\text{appr}}$ ,  $F_{a^2}^{\text{appr}}$  and  $F_W^{\text{appr}}$  yielding

$$\begin{aligned} R_\star &\rightarrow R_\star - \epsilon_r, & a^{\star 2} &\rightarrow a^{\star 2} - \epsilon_{a^2}, \\ u_H^\star &\rightarrow u_H^\star - \frac{\alpha_\star}{a^{\star 2}} \left( \frac{2R_0 a_0^2 W_0}{L^2} \epsilon_r + \frac{W_0}{\alpha_0^2} \epsilon_{a^2} + \frac{a_0^2}{\alpha_0^2} \epsilon_W \right), \end{aligned} \quad (42)$$

and a new run begins. The process is stopped when the criterion (41) is reached. As an example, for one helical vortex with  $\Gamma = 1$ ,  $L = 0.2$ ,  $R_0 = 1$ ,  $a_0 = 0.1$  and  $W_0 = 0$ , the process converges in two iterations, the errors are displayed in table 1.

**Table 1** Evolution of the distance to prescribed values at the end of each iteration while generating the base state BS1 (see table 2).

iteration	1	2
$\epsilon_r/R_0$	$3.4185 \cdot 10^{-3}$	$1.3762 \cdot 10^{-6}$
$\epsilon_{a^2}/a_0^2$	$1.4555 \cdot 10^{-2}$	$1.1959 \cdot 10^{-4}$
$\epsilon_W$	$1.0295 \cdot 10^{-3}$	$8.0407 \cdot 10^{-5}$

### 3.5 Base flow: examples

In the following, we present cases of base flow structures. Velocity and vorticity in this inertial frame are denoted as  $\mathbf{u}^{\text{BF}}$  and  $\boldsymbol{\omega}^{\text{BF}}$ . The values of the base flow parameters are listed in table 2. Regarding numerical parameters in plane  $\Pi_0$ , the radial mesh discretisation is regular with  $N_r = 768$  points between the center and the outer boundary at radius  $R_{\text{ext}} = 2$ . Azimuthally, we use here  $N_\theta = 384$  modes.

A first case (BS1) is characterized by no inner jet component ( $W_0 = 0$ , infinite swirl). It is displayed in figure 3. As expected, the component of velocity normal to the  $\Pi_\perp$ -plane, that is  $u_b$ , is very close to uniform in the vortex core (see figures 3b and e). However, the helical velocity component  $u_H$  is not and has a small negative amplitude, as observed on graph 3a; these negative values are counterbalanced by the projection of  $u_\varphi$  on  $\mathbf{e}_b$  to yield a uniform output.

The two other cases (BS2 and BS3) respectively displayed in figures 4 and 5 possess an inner jet component, either negative or positive, as clearly seen on the graphs 4e and 5e.

**Table 2** Dimensionless parameters for base states.

	BS1	BS2	BS3
$L$	0.2	0.3	0.7
$a_0$	0.1	0.11	0.15
$W_0$	0	-0.23	0.2

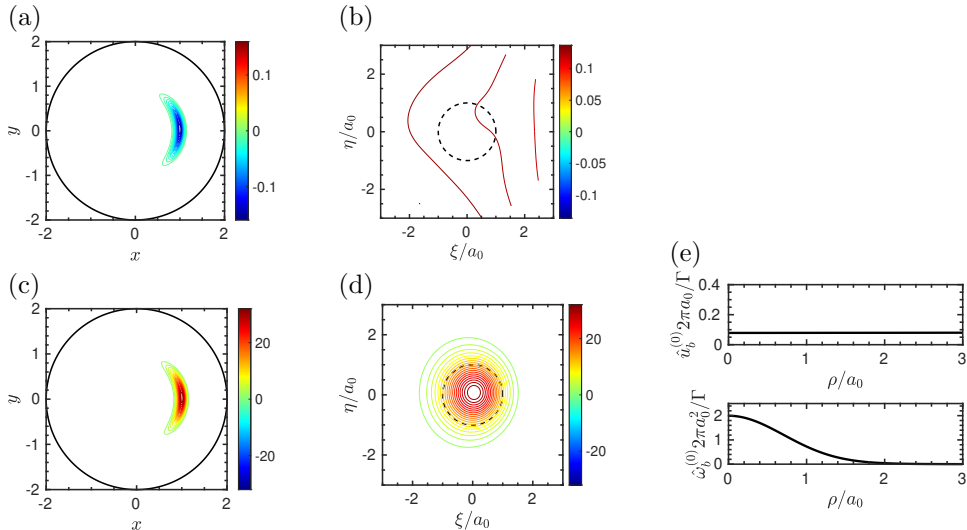


**Fig. 3** Base state BS1 ( $L = 0.2$ ,  $a_0 = 0.1$ ,  $W_0 = 0$ ): (a) velocity component  $u_H(r, \varphi)$  in  $\Pi_0$ ; (b)  $u_b(\rho, \psi)$  in  $\Pi_\perp$ ; (c) vorticity component  $\omega_B(r, \varphi)$  in  $\Pi_0$ ; (d)  $\omega_b(\rho, \psi)$  in  $\Pi_\perp$ ; (e) radial profiles of  $\hat{u}_b^{(0)}(\rho)$  and  $\hat{\omega}_b^{(0)}(\rho)$ . For isocontours, 20 regularly spaced levels are used in the positive range of values and 20 in the negative range.

## 4 Stability of a helically symmetric base state using helical variables

We now look for the stability of the base flow that was computed in the previous section. In the frame (R) rotating at angular velocity  $\Omega_0 \mathbf{e}_z$ , the base flow is

$$\mathbf{u}^{\text{BF(R)}} = \mathbf{u}^{\text{BF}} - \Omega_0 r \mathbf{e}_\theta, \quad \boldsymbol{\omega}^{\text{BF(R)}} = \boldsymbol{\omega}^{\text{BF}} - 2\Omega_0 \mathbf{e}_z. \quad (43)$$

It is thus steady up to viscous diffusion. Since disturbances superimposed on the quasi-equilibrium state evolve on a much faster time scale than the diffusion time, we assume that viscous diffusion can be neglected for the vortex base state only. Following a standard procedure in wakes and shear layers, we introduce a body force to suppress the viscous diffusion of the base flow in a clean mathematical way. In the rotating frame (R), the Navier–Stokes equations read

$$\partial_t \mathbf{u}^{(\text{R})} + \mathbf{NL} = -\nabla G^{(\text{R})} + \frac{1}{Re} \Delta \mathbf{u}^{(\text{R})} - \frac{1}{Re} \Delta \mathbf{u}^{\text{BF(R)}}, \quad (44)$$

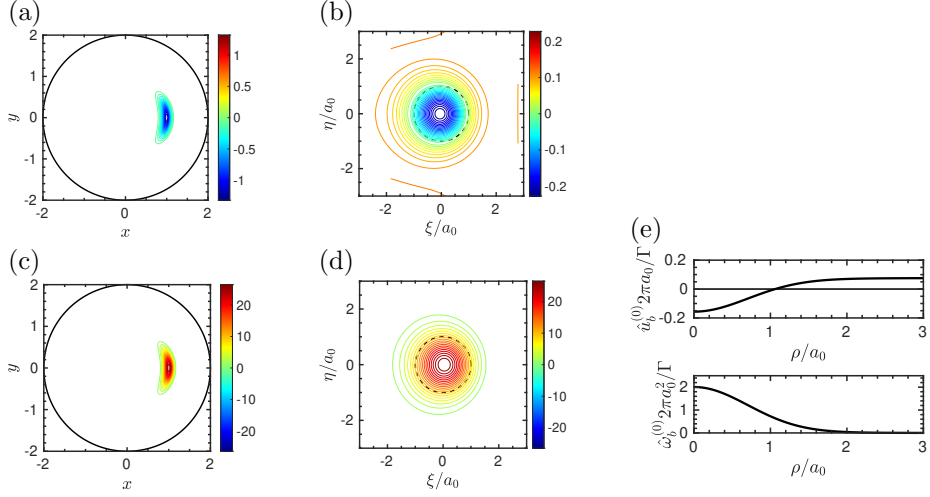


**Fig. 4** Same as figure 3, but for base state BS2 ( $L = 0.3$ ,  $a_0 = 0.11$ ,  $W_0 = -0.23$ ).

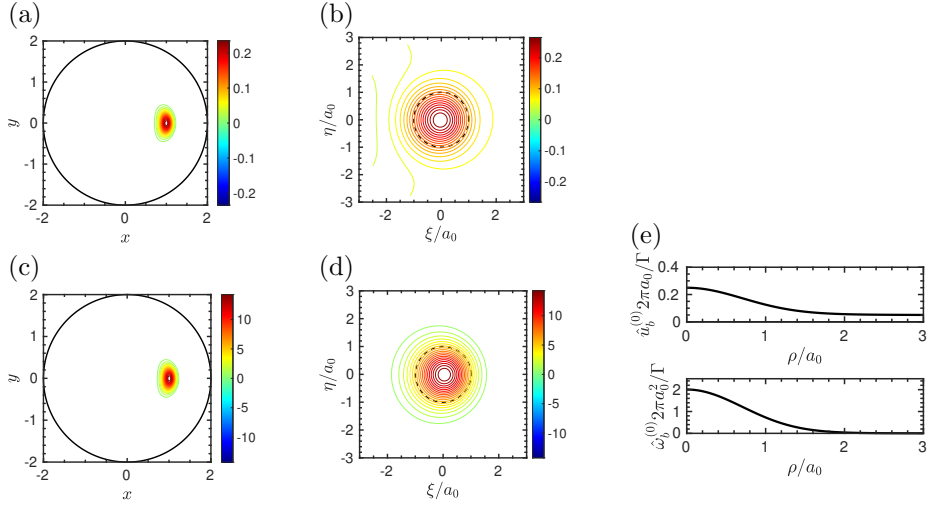


**Fig. 5** Same as figure 3, but for base state BS3 ( $L = 0.7$ ,  $a_0 = 0.15$ ,  $W_0 = 0.2$ ).

$$\nabla \cdot \mathbf{u}^{(R)} = 0, \quad (45)$$

with  $\mathbf{NL} \equiv \boldsymbol{\omega}^{(R)} \times \mathbf{u}^{(R)} + 2\Omega_0 \mathbf{e}_z \times \mathbf{u}^{(R)}$ .

#### 4.1 Linearized solver HELIKZ-LIN

The different fields are the sum of the base state and of a perturbation of order  $\epsilon \ll 1$ :

$$\mathbf{u}^{(R)}(r, \varphi, z, t) = \mathbf{u}^{\text{BF}(R)}(r, \varphi) + \epsilon \mathbf{u}'(r, \varphi, z, t),$$

$$\begin{aligned}\boldsymbol{\omega}^{(\text{R})}(r, \varphi, z, t) &= \boldsymbol{\omega}^{\text{BF(R)}}(r, \varphi) + \epsilon \boldsymbol{\omega}'(r, \varphi, z, t), \\ p^{(\text{R})}(r, \varphi, z, t) &= p^{\text{BF(R)}}(r, \varphi) + \epsilon p'(r, \varphi, z, t).\end{aligned}\quad (46)$$

Keeping only the terms of order  $\epsilon$ , one obtains the linear system governing perturbations, that is incompressibility  $\nabla \cdot \mathbf{u}' = 0$  and the linearized momentum equation

$$\partial_t \mathbf{u}' + \mathbf{LNL} = -\nabla G' + \frac{1}{Re} \mathbf{VT}, \quad (47)$$

where

$$\mathbf{LNL} \equiv \boldsymbol{\omega}^{\text{BF}} \times \mathbf{u}' + \boldsymbol{\omega}' \times \mathbf{u}^{\text{BF(R)}}, \quad G' \equiv \frac{p'}{\rho_{\text{fl}}} + \mathbf{u}^{\text{BF(R)}} \cdot \mathbf{u}', \quad \mathbf{VT} \equiv \Delta \mathbf{v}'. \quad (48)$$

In cylindrical basis  $(\mathbf{e}_r, \mathbf{e}_\theta, \mathbf{e}_z)$  with helical coordinates, incompressibility reads as

$$\nabla \cdot \mathbf{u}' = \frac{1}{r} \frac{\partial(r u'_r)}{\partial r} + \frac{1}{r} \frac{\partial u'_\theta}{\partial \varphi} + \frac{\partial u'_z}{\partial z} - \frac{1}{L} \frac{\partial u'_z}{\partial \varphi} = 0 \quad (49)$$

and components of linear terms  $\mathbf{LNL}$  as

$$\begin{aligned}\text{LNL}_r &\equiv \omega'_\theta u_z^{\text{BF(R)}} + \omega_\theta^{\text{BF}} u'_z - \omega'_z u_\theta^{\text{BF(R)}} - \omega_z^{\text{BF}} u'_\theta, \\ \text{LNL}_\theta &\equiv \omega'_z u_r^{\text{BF(R)}} + \omega_z^{\text{BF}} u'_r - \omega'_r u_z^{\text{BF(R)}} - \omega_r^{\text{BF}} u'_z, \\ \text{LNL}_z &\equiv \omega'_r u_\theta^{\text{BF(R)}} + \omega_r^{\text{BF}} u'_\theta - \omega'_\theta u_r^{\text{BF(R)}} - \omega_\theta^{\text{BF}} u'_r.\end{aligned}\quad (50)$$

Because the base state does not depend on  $z$ , the linear system (47) is not explicitly dependent on  $z$ . Hence, we may restrict the study to modes

$$\begin{pmatrix} u'_r \\ u'_\theta \\ u'_z \\ G' \end{pmatrix} = \begin{pmatrix} \tilde{u}_r(r, \varphi, t) \\ \tilde{u}_\theta(r, \varphi, t) \\ \tilde{u}_z(r, \varphi, t) \\ \tilde{G}(r, \varphi, t) \end{pmatrix} \exp(ik_z z) \quad (51)$$

characterized by a single real axial wavelength  $k_z$ , along the  $z$ -axis. Since the base state does not depend on  $t$ , the linear system (47) is not explicitly dependent on  $t$  and we could also restrict the study to modes

$$\begin{pmatrix} u'_r \\ u'_\theta \\ u'_z \\ G' \end{pmatrix} = \begin{pmatrix} \tilde{u}_r(r, \varphi) \\ \tilde{u}_\theta(r, \varphi) \\ \tilde{u}_z(r, \varphi) \\ \tilde{G}(r, \varphi) \end{pmatrix} \exp[i(k_z z - \varpi t)], \quad (52)$$

where the frequency  $\varpi = \omega + i\sigma$  is a complex containing the real frequency  $\omega$  and the growthrate  $\sigma$ . Introducing ansatz (52) into equation (47) transforms these governing equations into an eigenvalue problem which is in practice too large to be solved. As a consequence, we compute the most unstable mode of axial wavelength  $k_z$  by a different

approach: we simulate equations (47) starting with initial conditions of the form (51) with complex velocity perturbations consisting of colored noise in the region of nonzero basic vorticity (see appendix D.2). The most unstable mode is expected to emerge after a sufficiently long time from this initial noise since by definition its amplitude increases with the maximum growth rate among the set of waves of wavenumber  $k_z$ . The assumed expression (51) imposes the derivative  $\partial/\partial z$  in the linearized Navier–Stokes equations (47)–(49) to reduce to a multiplication by  $ik_z$ . Furthermore, quantities are  $2\pi$  periodic in the  $\varphi$  direction and can be expanded using a Fourier decomposition along  $\varphi$ :

$$\begin{pmatrix} \tilde{u}_r(r, \varphi, t) \\ \tilde{u}_\theta(r, \varphi, t) \\ \tilde{u}_z(r, \varphi, t) \\ \tilde{G}(r, \varphi, t) \end{pmatrix} = \sum_{n=-\infty}^{+\infty} \begin{pmatrix} \hat{u}_r^{(n)}(r, t) \\ \hat{u}_\theta^{(n)}(r, t) \\ \hat{u}_z^{(n)}(r, t) \\ \hat{G}^{(n)}(r, t) \end{pmatrix} \exp(in\varphi), \quad (53)$$

where quantities  $\hat{u}^{(n)}$  are complex and no relation exists between mode  $(-n)$  and mode  $n$ . Introducing expressions (53) into equations (47)–(49), yields for each mode  $n$ :

$$\nabla \cdot \hat{\mathbf{u}}^{(n)} = 0, \quad (54)$$

$$\frac{\partial \hat{\mathbf{u}}^{(n)}}{\partial t} + \mathbf{LNL}^{(n)} = -\nabla \hat{G}^{(n)} + \frac{1}{Re} \mathbf{VT}^{(n)}, \quad (55)$$

where linear operators take simpler expressions in modal form:

$$\nabla \cdot \hat{\mathbf{u}}^{(n)} = \frac{1}{r} \frac{\partial(r\hat{u}_r^{(n)})}{\partial r} - i \frac{n}{r} \hat{u}_\theta^{(n)} + i\beta \hat{u}_z^{(n)}, \quad (56)$$

$$\nabla \hat{G}^{(n)} = \left( \frac{\partial \hat{G}^{(n)}}{\partial r}, \frac{in}{r} \hat{G}^{(n)}, i\beta \hat{G}^{(n)} \right), \quad (57)$$

$$\begin{aligned} \mathbf{VT}_r^{(n)} &= \frac{\partial}{\partial r} \left( \frac{1}{r} \frac{\partial(r\hat{u}_r^{(n)})}{\partial r} \right) - \chi^2 \hat{u}_r^{(n)} - i \frac{2n}{r^2} \hat{u}_\theta^{(n)}, \\ \mathbf{VT}_\theta^{(n)} &= \frac{\partial}{\partial r} \left( \frac{1}{r} \frac{\partial(r\hat{u}_\theta^{(n)})}{\partial r} \right) - \chi^2 \hat{u}_\theta^{(n)} - i \frac{2n}{r^2} \hat{u}_r^{(n)}, \\ \mathbf{VT}_z^{(n)} &= \frac{1}{r} \frac{\partial}{\partial r} \left( r \frac{\partial \hat{u}_z^{(n)}}{\partial r} \right) - \chi^2 \hat{u}_z^{(n)}, \end{aligned} \quad (58)$$

with

$$\beta(n, k_z) \equiv k_z - \frac{n}{L}, \quad \chi^2(n, k_z) \equiv \frac{n^2}{r^2} + \beta^2. \quad (59)$$

The vorticity field is expressed as

$$\boldsymbol{\omega} = (\hat{\omega}_r^{(n)}, \hat{\omega}_\theta^{(n)}, \hat{\omega}_z^{(n)}) \exp[i(n\varphi + k_z z)], \quad (60)$$

with

$$\begin{aligned}
\hat{\omega}_r^{(n)} &= \frac{in}{r} \hat{u}_z^{(n)} - i\beta \hat{u}_\theta^{(n)}, \\
\hat{\omega}_\theta^{(n)} &= i\beta \hat{u}_r^{(n)} - \frac{\partial \hat{u}_z^{(n)}}{\partial r}, \\
\hat{\omega}_z^{(n)} &= \frac{1}{r} \frac{\partial}{\partial r} (r \hat{u}_\theta^{(n)}) - \frac{in}{r} \hat{u}_r^{(n)}.
\end{aligned} \tag{61}$$

In this approach, the three components of term  $\mathbf{LNL}^{(n)}$  are determined by using a standard pseudo-spectral method. Boundary conditions must be satisfied at  $r = \infty$  and  $r = 0$ . We assume that the flow is potential and decreasing when  $r \rightarrow \infty$ . The velocity field can be hence expressed as a gradient of a solution of Laplace equation. For each mode, the potential  $\Phi^{(n)}$  can be easily shown to satisfy after rescaling a modified Bessel equation of the second kind [25]. Using the decreasing solution at  $r \rightarrow \infty$ , this imposes

$$\Phi^{(n)} = BK_{|n|}(|\beta|r), \tag{62}$$

where  $K_{|n|}(\hat{r})$  is a modified Bessel function of the second kind [25].

The boundary conditions at  $r = 0$  originate from regularity considerations at the axis [26]: for a scalar field  $f$ , the Fourier coefficient as  $r \rightarrow 0$  reads  $f^{(n)}(r) \sim r^{|n|} F_n(r)$  where  $F_n(r)$  is a regular even function. For a vector field  $\mathbf{v}$ ,  $v_r^{(0)}$  vanishes and the components satisfy  $v_\theta^{(0)} = rD_0(r)$  and  $v_z^{(0)} = V_0(r)$  where  $D_0(r)$  and  $V_0(r)$  are even complex functions. The boundary conditions at  $r = 0$  read:

$$v_\theta^{(0)} = 0, \quad \frac{\partial v_z^{(0)}}{\partial r} = 0 \quad \text{at } r = 0. \tag{63}$$

For  $|n| \geq 1$ , regularity imposes that  $v_r^{(n)} = \frac{1}{2}(v_+^{(n)} + v_-^{(n)})$  and  $v_\theta^{(n)} = \frac{1}{2i}(v_+^{(n)} - v_-^{(n)})$  with

$$v_+^{(n)}(r) \sim r^{|n|+1} G_+^n(r), \quad v_-^{(n)}(r) \sim r^{|n|-1} G_-^n(r), \tag{64}$$

where  $G_+^n(r)$  and  $G_-^n(r)$  are even functions. For  $|n| = 1$ , equations (64) indicate that

$$\frac{\partial v_r^{(\pm 1)}}{\partial r} = 0, \quad \frac{\partial v_\theta^{(\pm 1)}}{\partial r} = 0, \quad v_z^{(\pm 1)} = 0 \quad \text{at } r = 0. \tag{65}$$

For  $|n| > 1$ , Dirichlet conditions are obtained for all the velocity components:

$$v_r^{(n)} = 0, \quad v_\theta^{(n)} = 0, \quad v_z^{(n)} = 0 \quad \text{at } r = 0. \tag{66}$$

Details about discretization of this system can be found in appendix D.

## 4.2 Most unstable mode extraction for a given wavenumber $k_z$

The time evolution using the solver HELIKZ-LIN is shown in figure 6 for a case of short wavelength instability mode of  $k_z = 20$ , up to final time  $T_{\text{sim}} = 150$ . The growth

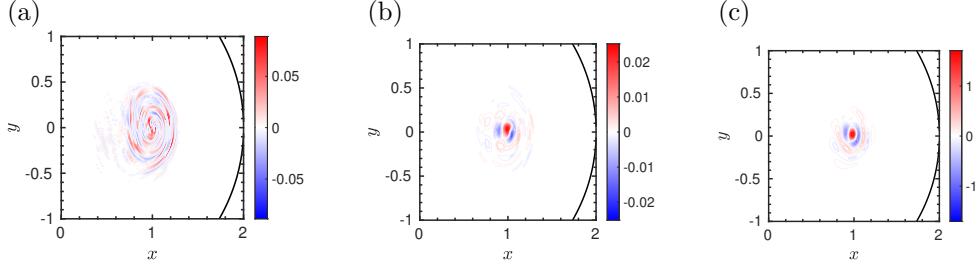


**Fig. 6** Perturbation initialized with noise (see figure D2). Real part of axial vorticity  $\omega'_z$  after evolution at (a)  $t = 5$ , (b)  $t = 30$  and (c)  $t = 150$ . Example taken from the case of BS3 computed by the helical simulation.

rate is extracted from the temporal evolution of the norm  $E_c$  based on kinetic energy

$$E_c \equiv \int_{\Pi_0} (\tilde{u}_r \tilde{u}_r^\dagger + \tilde{u}_\theta \tilde{u}_\theta^\dagger + \tilde{u}_z \tilde{u}_z^\dagger) r \, dr \, d\varphi, \quad (67)$$

where  $\dagger$  stands for complex conjugate. As the most unstable mode grows exponentially as  $\exp[(\sigma - i\omega)t]$ ,  $E_c(t)$  grows as  $\exp(2\sigma t)$ . We then estimate the growth rate as follows. During the simulation, we compute the quantity

$$\sigma(t) = \frac{1}{2} \frac{\ln[E_c(t)/E_c(t - \Delta t)]}{\Delta t} \quad (68)$$

at times  $t_n = n\Delta t$  with  $\Delta t = 0.5$  and  $n = 1, 2, \dots$ . The simulation is stopped when  $\sigma(t_n)$ ,  $\sigma(t_{n-1})$  and  $\sigma(t_{n-2})$  mutually differ by less than  $5 \cdot 10^{-5}$  (or  $10^{-5}$  in some cases), which indicates that  $\ln E_c$  varies linearly in time within this precision. When this is reached, the value of  $\sigma(t_n)$  yields  $\sigma_{\text{hel}}$ . In figure 7a, one displays the norm  $E_c$  as a function of time (black curve). The energy first decreases as the initial perturbation contains also damped modes, then the most unstable mode emerges and dominates the evolution. In this example, the growthrate is  $\sigma_{\text{hel}} = 3.638 \cdot 10^{-2}$  (red dashed curve).

In order to determine the mode frequency  $\omega_{\text{hel}}$  in the rotating frame, the normalized velocity component

$$\tilde{u}_z(r, \varphi, t) = \frac{\tilde{u}_z(r, \varphi, t)}{\left( \iint |\tilde{u}_z(r, \varphi, t)|^2 r \, dr \, d\varphi \right)^{1/2}}$$

is computed at two different times  $t_1$  and  $t_2$  typically, with  $\delta t' \equiv t_2 - t_1 = 0.02$  — a small value being necessary so as to avoid periodicity effects. Since it is expected that

$$\tilde{u}_z(r, \varphi, t_2) = \tilde{u}_z(r, \varphi, t_1) \exp[-i\omega_{\text{hel}}(t_2 - t_1)], \quad (69)$$

we determine the frequency based on the best correlation between  $\tilde{u}_z(r, \varphi, t_1) \exp(-i\omega\delta t')$  and  $\tilde{u}_z(r, \varphi, t_2)$  over the whole  $\Pi_0$  plane. The complex

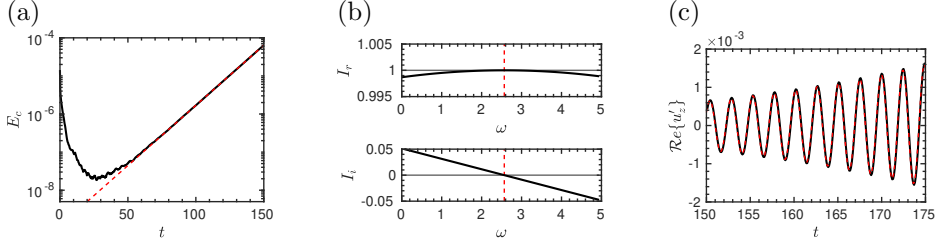


**Fig. 7** Perturbation initialized in figure D2. (a) Temporal evolution of energy  $E_c$  (solid curve) and exponential growth (red dashed corresponding to the growth rate obtained by eq. (68)). (b) Real and imaginary parts of the correlation coefficient  $I(\omega)$  given by equation (70) (solid curves) and the deduced frequency (red dashed). (c) Temporal evolution of the real part of perturbation  $v'_z$  at point A in plane  $\Pi_0$  in the linear regime (black solid line) as a final check for assessing the values  $\sigma_{\text{hel}}$  and  $\omega_{\text{hel}}$  obtained in (a)–(b), represented by the colored dashed line. Example taken from the case of BS3 computed by the helical simulation.

correlation coefficient

$$I(\omega) = \iint \tilde{u}_z(r, \varphi, t_1) e^{-i\omega\delta t'} \tilde{u}_z^\dagger(r, \varphi, t_2) r \, dr \, d\varphi, \quad (70)$$

would satisfy  $I(\omega_{\text{hel}}) = 1$  for a perfect correlation; we obtain the frequency by requiring that  $I(\omega_{\text{hel}})$  be real, i.e.  $\omega_{\text{hel}} = \arg[I(0)]/\delta t'$ . In figure 7b, one displays the correlation coefficient  $I(\omega)$ , the imaginary part of which vanishes for the frequency value  $\omega_{\text{hel}} = 2.567$ . The validity of the procedure is confirmed in figure 7c.

The complex instability mode obtained through the linear simulation via the solver HELIKZ-LIN is characterized by velocity components  $\tilde{u}_r, \tilde{u}_\theta, \tilde{u}_z$  or vorticity components  $\tilde{\omega}_r, \tilde{\omega}_\theta, \tilde{\omega}_z$  in the plane  $\Pi_0$ . It is relevant to display these fields in the section orthogonal to the vortex filament, that is in the plane  $\Pi_\perp$ . Indeed in the asymptotic limit where the core size of the vortex is small compared to its radius of curvature, one may study the various instabilities occurring on a helical vortex based on an expansion around the case of a straight vortex [6, 7]. To compare the structure of the modes found with this asymptotic case, it is clear that the mode structure in the plane  $\Pi_\perp$  is required. To do so, we use the method applied in §3.3 for base flows and, in addition, take into account a phase shift between point  $M_0 \in \Pi_0$  and point  $M_\perp \in \Pi_\perp$  on the same helical line but separated along the axis by  $\Delta z = z_{M_\perp} - z_{M_0}$  (see figure 2b). This projection process is illustrated in figure 8. Finally, we adopt the local polar coordinates  $(\rho, \psi)$  of axis normal to the plane  $\Pi_\perp$  of center point A (this axis defines the  $b$ -component). The spatial structure of the mode in the plane  $\Pi_\perp$  is obtained by applying a Fourier decomposition along  $\psi$ :

$$\hat{u}^{(m)}(\rho) = \frac{1}{2\pi} \int_0^{2\pi} \tilde{u}(\rho, \psi) e^{-im\psi} d\psi, \quad (71)$$

where  $m$  denotes the local azimuthal wavenumber in plane  $\Pi_\perp$ . As for normalization, we look for the maximum modulus of  $\hat{u}_b^{(m)}(\rho)$  over all radial stations  $\rho$  and all  $m$  values. Any quantity  $u^{(m)}(\rho)$  is then divided by the corresponding complex value of  $\hat{u}_b^{(m)}(\rho)$ .

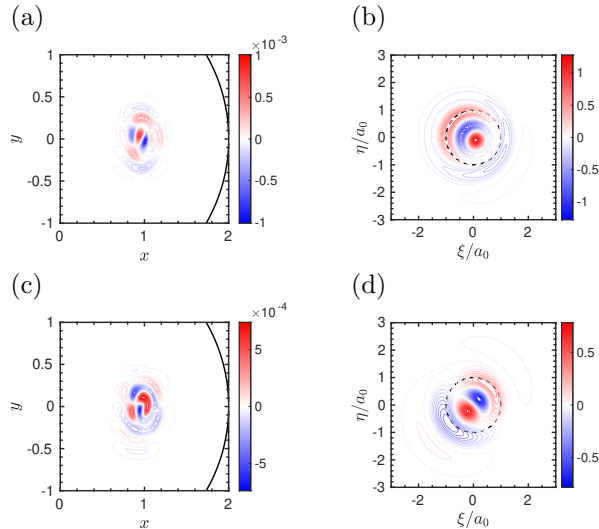


**Fig. 8** Velocity perturbation: contours for the real part of (a)  $u'_B(r, \varphi)$  in plane  $\Pi_0$  zoomed on the perturbation, and (b)  $u'_b(\rho, \psi)$  in plane  $\Pi_\perp$ . (c) and (d): contour plots of the companion imaginary parts. Note that  $u'_b$  has been normalized. Example taken from the case of BS3 computed by the helical simulation.

## 5 Instability of a helically symmetric base state using three-dimensional simulations

The validity of the above procedure is checked against a more classical approach consisting in three-dimensional linearized simulations in cylindrical coordinates, as previously used in the context of vortex-ring instabilities [8]. We solve the linearized Navier–Stokes equations

$$\frac{\partial \mathbf{u}'}{\partial t} + \mathbf{u}^{\text{BF(T)}} \cdot \nabla \mathbf{u}' + \mathbf{u}' \cdot \nabla \mathbf{u}^{\text{BF(T)}} = -\nabla p' + \nu \nabla^2 \mathbf{u}', \quad (72)$$

$$\nabla \cdot \mathbf{u}' = 0, \quad (73)$$

in the inertial frame in which the base flow is steady. In this frame, the base velocity field reads  $\mathbf{u}^{\text{BF(T)}} = \mathbf{u}^{\text{BF}} - U_0 \mathbf{e}_z$ , where  $U_0 = -\Omega_0 L$ , and differs from that of the base flow (43) in the rotating frame employed in §4. We discretize equations (72) and (73) in the cylindrical coordinate system with  $r \leq R_{\text{far}} = 100$  and  $z \in [0, L_{\text{box}}]$  where  $L_{\text{box}} = n_p \times 2\pi L$  is an integer number  $n_p$  of helix pitch. For the spatial discretization, the sixth-order accurate compact scheme [27] is used in the  $r$  direction, while the Fourier spectral method is used in the  $\theta$  and  $z$  directions, in which the periodic boundary conditions are imposed. The singularity at  $r = 0$  is avoided by expanding the  $r$  axis to  $-R_{\text{far}} \leq r \leq R_{\text{far}}$ , where the radial boundary is placed at  $R_{\text{far}}$ , and placing no grid point at  $r = 0$ . The slip boundary conditions

$$u'_r = 0, \quad \frac{\partial}{\partial r}(ru'_\theta) = \frac{\partial}{\partial r}u'_z = 0 \quad (74)$$

are imposed at  $r = R_{\text{far}}$ . For the temporal discretization, the Crank–Nicolson scheme is used for the viscous terms, while the second-order Adams–Bashforth method is used for the other terms. The discretized equations are shown in some detail in Appendix E.1. The Poisson equations, which appear in the formulation in Appendix E.1, can be decomposed into a set of ordinary differential equations for a single Fourier mode; they are also solved by a sixth-order accurate compact scheme. Non-uniform stretched grids are used in the  $r$  direction; the grid size at  $r = R_{\text{far}}$  is  $\Delta r = 2$ , while it is smaller than  $5 \times 10^{-3}$  for  $r < 1.94$ . The numbers of grid points in the  $r$  and  $\theta$  directions are  $N_r = 695$  and  $N_\theta = 1280$ , respectively, while the number of grid points in the  $z$  direction is  $N_z = 384$  and  $768$  for  $L/R = 0.3$  and  $0.7$ , respectively.

We use the base flows obtained in section 3, *via* the helical simulation. For  $r \leq R_{\text{ext}} = 2$ , the base state is obtained through interpolation of helical fields on the non-uniform grid points. For  $R_{\text{ext}} = 2 \leq r \leq R_{\text{far}}$ , it is necessary to extrapolate the base flow from  $R_{\text{ext}}$  to  $R_{\text{far}}$ . This is possible since the base flow is potential in that region, and can be explicitly written in terms of Bessel functions.

Since we want to reproduce the computation of a single mode of the form (51) characterized by a single real axial wavelength  $k_z$  along the  $z$ -axis, this imposes, in the 3D setting, an integer number  $p$  of wavelengths within the size of the box  $L_{\text{box}}$  that is  $p \times 2\pi/k_z = L_{\text{box}}$ . If  $n_p$  helix pitches are simulated within the numerical box, the available wavenumbers are  $k_z = p/(n_p L)$  with  $p = 1, 2, \dots$ . Using  $n_p > 1$  is more CPU demanding, but can be found necessary for two reasons. First, capturing long-wave instabilities in a single helical vortex requires using at least  $n_p = 2$  helix pitches, since the first long-wave instability corresponds to the mode such that  $k_z L = \frac{1}{2}$ . Second, for short-wave instabilities, wavenumbers  $k_z = p/L$  might all fall outside of the instability range in which a resonance arises.

The initial vorticity distribution of the disturbance is randomized and is concentrated in the vortex-core region. It is created along four steps: (i) a randomized scalar field along the  $\theta$  direction is generated for each velocity component; (ii) a mask is used to localize these fields in the region of the base helical vortex in two dimensions; (iii) the fields are made three-dimensional according to the expected behaviour of the instability modes; (iv) the obtained field is projected to a divergenceless field  $\mathbf{u}$ . Details are given in Appendix E.2.

The growth rate is extracted from the temporal evolution of the kinetic energy integrated over the whole computational domain, which is equivalent to the procedure followed in the complex helical framework since the mode is of the form (51). The frequency is obtained by representing the quantity  $\hat{u}_b^{(m)}(\rho, t)$  for one of the dominant azimuthal contributions  $m$  in the complex plane at successive times separated by  $\Delta t$  (see figure 9, where  $\Delta t = 0.25$ ). From one selected time to the next, this representation rotates by an angle of  $\omega_{3D}\Delta t$  since  $\hat{u}_b^{(m)}$  is proportional to  $\exp[(\sigma_{3D} + i\omega_{3D})t]$ . This allows one to obtain  $\omega_{3D}$  in the translating frame; in order to compare it with the frequency  $\omega_{\text{hel}}$  obtained in section 4 which is in the rotating frame, we must take the Doppler shift into account by adding  $k_z U_0$ .

The spatial structure of the instability mode is represented in figure 10a using isosurfaces of  $\omega'_B$ . For the sake of comparison with helical results, figure 10b presents isocontours plots of  $u'_b$  in two  $\Pi_\perp$ -planes, in perfect agreement with the real and

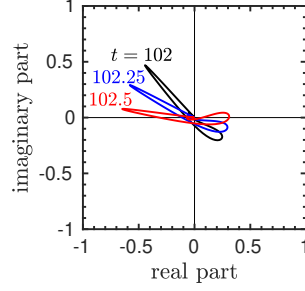


**Fig. 9** Complex quantity  $\hat{u}_b^{(1)}(\rho, t)$  plotted in the complex plane for several values of  $t$  indicated in the graph. The representation rotates by an angle of  $\omega_{3D}\Delta t$  during  $\Delta t = 0.25$ , allowing to retrieve  $\omega_{3D}$ . Example taken from the case of BS3 computed by 3D simulation.

imaginary parts of the helical simulation (see figure 8b-d). This correspondance is indeed expected: assume that the 3D real simulation provides the value  $R_1(\rho, \psi)$  of  $u'_b$  in some plane  $\Pi_\perp(z_0)$ , and provides  $R_2(\rho, \psi)$  at  $\Pi_\perp(z_0 + \lambda/4)$ . Since the instability mode is of the form (51) and any point  $(\rho, \psi)$  in  $\Pi_\perp(z_0)$  has a companion in  $\Pi_\perp(z_0 + \lambda/4)$ , characterized by same  $(r, \varphi)$  but  $z$  locations differing by  $\lambda/4$ , this is enough to reconstruct the complex mode  $\tilde{u}'_b \propto R_1(\rho, \psi) - iR_2(\rho, \psi)$  in a  $\Pi_\perp$  plane up to a complex normalization constant determined as for helical computations (see §4.2).

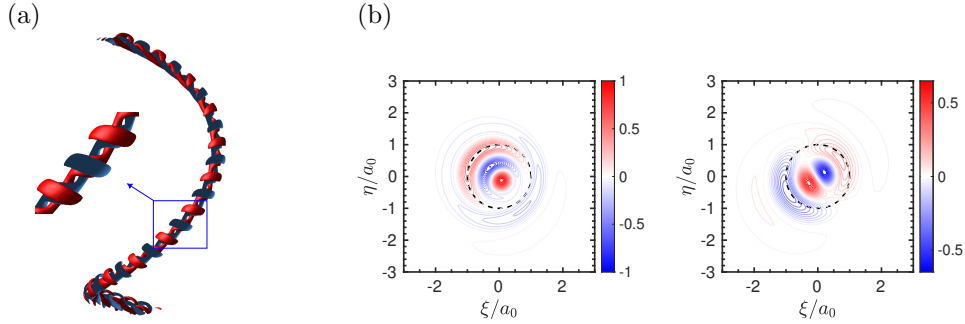


**Fig. 10** Instability mode structure: (a) isosurfaces of vorticity component  $\omega'_B$ ; (b) isocontours of velocity component  $u'_b$  in two  $\Pi_\perp$  planes distant by  $\lambda/4$  along  $z$ . Example taken from the case of BS3 computed by 3D simulation.

## 6 Some instability modes of helical vortices

Results are illustrated on three typical modes generated by three different instability mechanisms. The first case is a long-wave instability mode (axial wavenumber  $k_z = 2.5$ , that is  $k_z L = 0.5$ ) developing on base state BS1. The second case is a short-wave mode (axial wavenumber  $k_z = 106.6$ , that is  $k_z L = 32$ ) produced by the elliptical instability on base state BS2. The third case is a short-wave mode (axial wavenumber  $k_z = 20$ , that is  $k_z L = 14$ ) produced by the curvature instability on base state BS3. Growth rates and frequencies computed via the helical simulation method and via the fully

three-dimensional approach for BS1, BS2 and BS3 are compared in table 3. Getting the growth rate and the frequency of a single mode typically requires 160h CPU time via the helical simulation, that is 10 hours on a 16 core desk computer. For the fully three-dimensional simulation, such a run can require 307200 CPU hours, that is 10 days on the 1280-core cluster AFI-NITY (Fujitsu Server, PRIMERGY CX2550M4).

**Table 3** Growth rates  $\sigma_{\text{hel}}$  as computed via the helical simulation method and  $\sigma_{3\text{D}}$  obtained via three-dimensional simulation, as well as corresponding frequencies  $\omega_{\text{hel}}$  and  $\omega_{3\text{D}} + k_z U_0$ .

$k_z$	BS1	BS2	BS3
$k_z$	2.5	106.67	20
$\sigma_{\text{hel}}$	0.505	0.227	$2.47 \cdot 10^{-2}$
$\sigma_{3\text{D}}$	0.505	0.227	$2.43 \cdot 10^{-2}$
$\omega_{\text{hel}}$	1.258	41.82	2.566
$\omega_{3\text{D}} + k_z U_0$	1.262	41.80	2.587

## 6.1 Mesh convergence

The simulation of instabilities in a helical vortex is a challenging task because of the different spatial scales present in the system. The convergence with respect to the grid size has thus to be examined carefully. The requirements on the grid size vary according to several base state parameters: a thinner vortex core  $a$  and/or a stronger inner jet amplitude requires a more refined mesh in both  $r$  and  $\varphi$  directions, while a larger pitch  $L$  requires a more refined mesh along  $\varphi$  only. Indeed, a vortex of core size  $a_0$  covers a radial range of extent  $a_0$ , while it covers an azimuthal range of  $a_0/(\alpha_0 R_0) = a_0(R_0^{-2} + L^{-2})^{1/2}$ , which increases as  $L$  decreases.

In table 3, the values of  $\sigma_{\text{hel}}$  and  $\omega_{\text{hel}}$  are not directly obtained from a single simulation, but are extrapolated from the results of several simulations on different grids. For the instabilities of BS2 and BS3, figure 11 shows the sensitivity of the results with respect to changes of  $N_r$  and  $N_\theta$ , or equivalently on the radial grid size  $h_r = R_{\text{ext}}/N_r$  and azimuthal grid size (at  $r = 1$ )  $h_\theta = 2\pi/N_\theta$ . Since the radial definition and the azimuthal definition seem to affect the results in an independent fashion, it seems reasonable to infer a dependency of the form:

$$\begin{aligned}\sigma(h_r, h_\theta) &= \sigma_{\text{hel}} + A_r h_r^{p_r} + A_\theta h_\theta^{p_\theta} + o(h_r^{p_r}) + o(h_\theta^{p_\theta}) \\ \omega(h_r, h_\theta) &= \omega_{\text{hel}} + B_r h_r^{q_r} + A_\theta h_\theta^{q_\theta} + o(h_r^{q_r}) + o(h_\theta^{q_\theta}),\end{aligned}\quad (75)$$

without any cross term in  $h_r^{l_r} h_\theta^{l_\theta}$ . In (75),  $A_r$ ,  $A_\theta$ ,  $B_r$ ,  $B_\theta$  are real prefactors, and  $p_r$ ,  $p_\theta$ ,  $q_r$ ,  $q_\theta$  are real exponents (*a posteriori* orders of the numerical approximation for the whole procedure). A nonlinear least-square fit of the numerical results with the above law leads to determine the various parameters, and in particular the Richardson extrapolated values  $\sigma_{\text{hel}}$  and  $\omega_{\text{hel}}$  obtained as  $h_r, h_\theta \rightarrow 0$ . Such procedure leads to

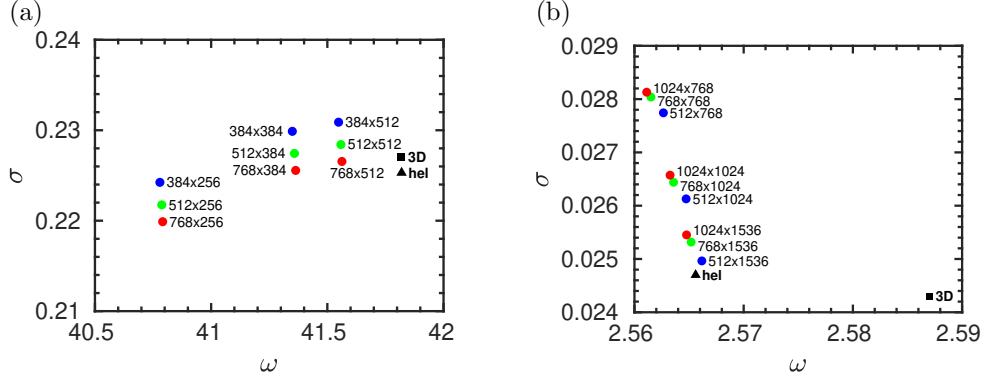


**Fig. 11** Influence of radial and azimuthal definitions on the numerical results for (a) the elliptic mode of BS2 and (b) the curvature mode of BS3 in the  $\omega$ - $\sigma$  plane: helical code (circles with grid size  $N_r \times N_\theta$ ), Richardson extrapolation from the helical results (black triangle) and 3D code (black square symbol).

a very good fit for the results of the instability in BS2, and we find  $\sigma_{\text{hel}} = 0.2253$ ,  $p_r = 1.82$ ,  $p_\theta = 3.89$  and  $\omega_{\text{hel}} = 41.8195$ ,  $q_r = 3.10$ ,  $q_\theta = 2.01$ . For BS3, we find  $\sigma_{\text{hel}} = 0.0247$ ,  $p_r = 1.82$ ,  $p_\theta = 2$  and  $\omega_{\text{hel}} = 2.566$ ,  $q_r = 2.03$ ,  $q_\theta = 1.96$ . The point  $(\omega_{\text{hel}}, \sigma_{\text{hel}})$  of such Richardson-extrapolated results is found, for BS2, to be located very close to the point  $(\omega_{3\text{D}}, \sigma_{3\text{D}})$  of the 3D simulation performed with a relatively fine grid (however with a different numerical formulation). For BS3 however, the agreement between helical and 3D simulations holds mainly for  $\sigma$ , a discrepancy of 1% is found for  $\omega$ .

In conclusion, the number of grid points along  $\theta$  seems to be of utmost importance here. It is recommended at least to use a Richardson extrapolation along  $\theta$ , or to use even finer grids in the azimuthal direction.

## 6.2 Case of long-wave instability mode

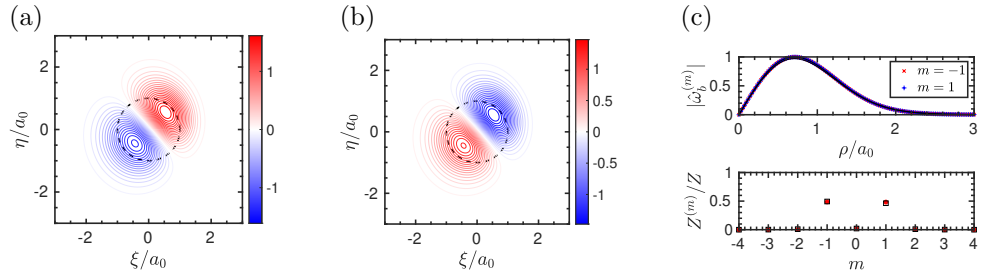


**Fig. 12** Long-wave mode  $k_z = 2.5$  for base state BS1 ( $L = 0.2$ ,  $a_0 = 0.1$ ,  $W_0 = 0$ ). (a) Isocontours in plane  $\Pi_\perp$  for the real part of  $\omega'_b(\rho, \psi)$  and (b) the imaginary part of  $\omega'_b(\rho, \psi)$ . (c) Top: radial structures of dominant azimuthal modes  $|\hat{\omega}_b^{(m)}|$  as functions of  $\rho/a_0$  (symbols: helical code, black line: 3D code); bottom: enstrophy ratios  $Z^{(m)}/Z$  (red circles: helical code, black squares: 3D code).

The first illustration is a long-wave instability in the single helical vortex base flow BS1. We use  $n_p = 2$  helix pitches in 3D simulations thus enabling wavenumber  $k_z = 1/(2L)$  which corresponds to the first long-wave mode. Long-wave modes are displacement modes, i.e. modes which tend to shift the vortex away from the baseline, without deforming the vortex core. To analyse such modes, it is more pertinent to use quantities relative to vorticity. Figures 12a-b display the real and imaginary part of the vorticity perturbation. The two lobes  $\pm$  are indeed typical of the structure of the displacement of a Gaussian vortex. We also consider enstrophy ratios  $Z^{(m)}/Z$  defined by

$$Z^{(m)} = \frac{1}{4} \int_0^\infty (|\hat{\omega}_\rho^{(m)}|^2 + |\hat{\omega}_\psi^{(m)}|^2 + |\hat{\omega}_b^{(m)}|^2) \rho d\rho, \quad Z \equiv \sum_m Z^{(m)}. \quad (76)$$

Such ratios reflect the distribution of energy over different azimuthal contributions, as shown here in the bottom graph of figure 12c. The radial structure of the dominant azimuthal contributions is shown in the top graph of figure 12c. This confirms that the longwave mode involves two symmetric displacement modes  $m = \pm 1$ , the radial structure being the derivative of a Gaussian base vorticity as expected. Furthermore, the agreement between helical and 3D simulation is excellent.

### 6.3 Case of elliptic mode

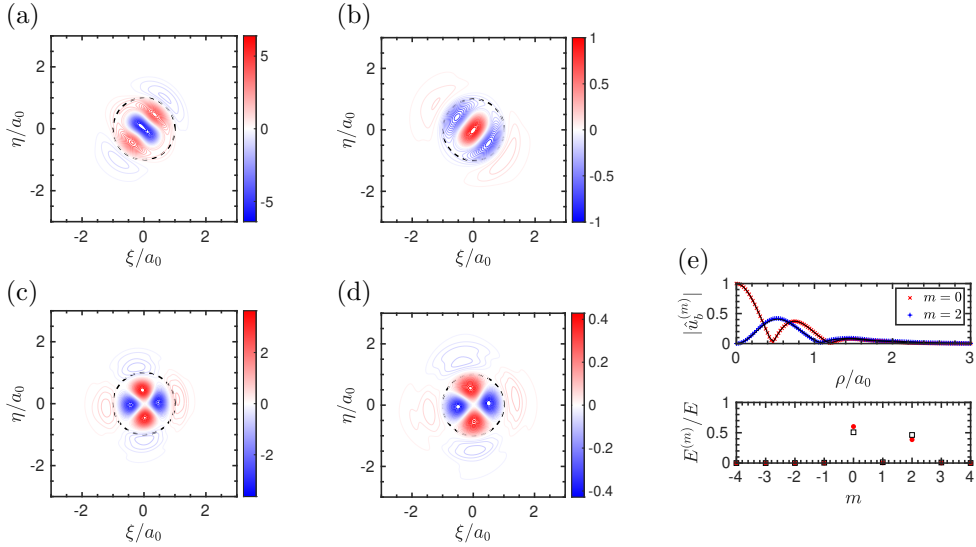


**Fig. 13** Elliptic mode with  $k_z = 106.67$  for base state BS2 ( $L = 0.3$ ,  $a_0 = 0.11$ ,  $W_0 = -0.23$ ). Isocontours in plane  $\Pi_\perp$  for (a) real part of  $\omega'_b(\rho, \psi)$ , (b) real part of  $u'_b(\rho, \psi)$ , (c) imaginary part of  $\omega'_b(\rho, \psi)$ , (d) imaginary part of  $u'_b(\rho, \psi)$ . (e) Top: radial structures of dominant azimuthal modes  $|\hat{u}_b^{(m)}|$  as functions of  $\rho/a_0$  (symbols: helical code, black line: 3D code); bottom: energy ratios  $E^{(m)}/E$  (red circles: helical code, black squares: 3D code).

The second illustration is a short-wave elliptic instability of the single helical vortex base flow BS2. Here, we use  $n_p = 1$  helix pitch in the 3D simulation. Results are displayed in figure 13. Graphs 13a and 13c show the real and imaginary part of the normal vorticity perturbation. The structure of the real part (graph a) is in agreement with the asymptotic study represented in figure 3b of Ref. [6] for a slightly different intensity of the inner jet parameter ( $W_0 = -0.2$  instead of  $-0.23$  here). Graphs 13b and 13d display the real and imaginary part of the normal velocity perturbation. As shown in graph 13e displaying energy ratios  $E^{(m)}/E$  and radial structures of the dominant azimuthal contributions, this mode stems from the resonance of two Kelvin waves at  $m = 0$  and  $m = 2$  excited by the elliptical deformation of the base flow. Results from the helical simulation and from the 3D one are found in close agreement with each other, as already discussed in §6.1.

#### 6.4 Case of curvature mode

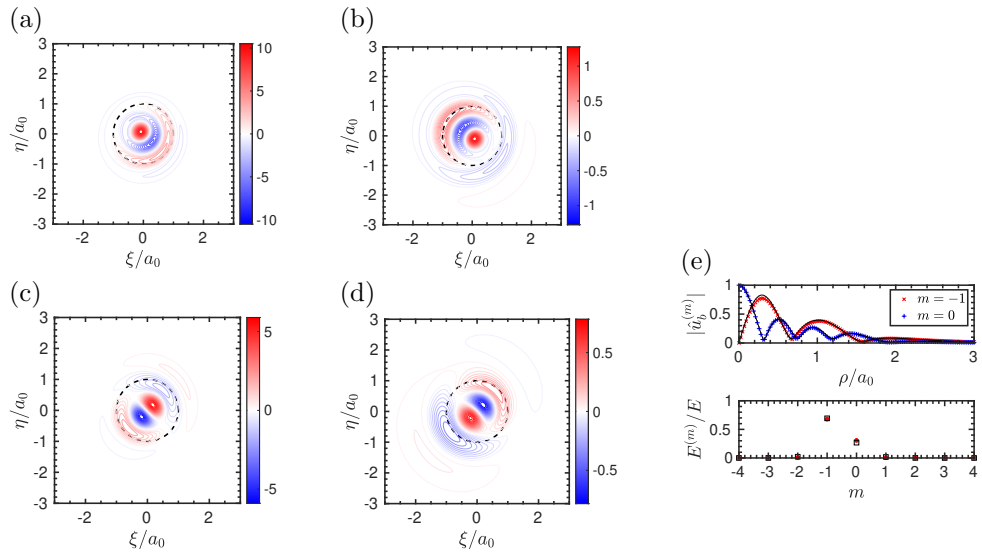


**Fig. 14** Curvature mode with  $k_z = 20$  for base state BS3 ( $L = 0.7$ ,  $a_0 = 0.15$ ,  $W_0 = 0.2$ ). Isocontours in plane  $\Pi_\perp$  for (a) real part of  $\omega'_b(\rho, \psi)$ , (b) real part of  $u'_b(\rho, \psi)$ , (c) imaginary part of  $\omega'_b(\rho, \psi)$ , (d) imaginary part of  $u'_b(\rho, \psi)$ . (e) Top: radial structures of dominant azimuthal modes  $|\hat{u}_b^{(m)}|$  as functions of  $\rho/a_0$  (symbols: helical code, black line: 3D code); bottom: energy ratios  $E^{(m)}/E$  (red circles: helical code, black squares: 3D code).

The last illustration is a short-wave curvature instability of the single helical vortex base flow BS3. We use  $n_p = 1$  helix pitch in the 3D simulation. Results are displayed in figure 14. Graphs 14a and 14c show the real and imaginary part of the normal vorticity perturbation. The structure of the real part (graph 14a) is in agreement with the asymptotic study represented in figure 7e of Ref. [7] for the same intensity of the inner jet parameter ( $W_0 = 0.2$ ). Graphs 14b and 14d display the real and imaginary

part of the normal velocity perturbation. Graph 14e demonstrates that this mode stems from the resonance of two Kelvin waves at  $m = -1$  and  $m = 0$ . Resonance is due here to vortex curvature, which shifts the core of the base flow vortex outwards (i.e. a  $m = 1$  excitation). Results from the helical simulation and from the 3D one are found in close agreement with each other, as discussed in §6.1.

## 7 Concluding remarks

In this paper, an original procedure aimed at numerically investigating the linear stability properties of a helical vortex is presented. It is based on the use of helical symmetry for the basic flow and plane axial waves for the disturbances, which makes it possible to simulate this three-dimensional system with a two-dimensional CPU cost. The procedure is assessed and fully validated against results from standard linearized three-dimensional computations.

The procedure involves two steps. In the first step, a quasi-equilibrium flow is computed using a Navier–Stokes solver HELIX via a generalized  $\psi - \omega$  formulation using helical variables and helical symmetry. An iterative procedure leads to a helical solution with prescribed parameter values: the helical pitch is enforced in the equations, the vortex circulation is imposed by the initial condition (a Gaussian helical vortex with circular core), so that the three remaining parameters (helical radius, core size and inner jet component) have to be iteratively corrected up to the desired state. Indeed, each iteration consists in a direct two-dimension-like simulation during which the three parameters evolve in a coupled manner towards a quasi-equilibrium state. This first step may be extended to generate states with multiple vortices with same pitch, in particular regularly interleaved helical vortex systems pertinent for rotor wake flows. A hub vortex may also be added, either helical with the same pitch, or axisymmetric since axisymmetric flows are also helically symmetric. For multiple vortices, additional treatments such as azimuthal filtering or selective frequency damping may be found necessary since such configurations are known to be unstable with respect to helically symmetric perturbations, especially at low pitch [11]. The second step consists in extracting the mode that dominates the linear instability of the above base flow, for a prescribed value of the axial wavenumber  $k_z$ . This is done using an original Navier–Stokes solver HELIKZ-LIN linearized in the vicinity of such helical state, using primitive complex variables and assuming a dependency of the perturbation fields in  $e^{ik_z z}$ . Starting from white noise or from an approximate solution (obtained for instance for a close enough set of parameters), the most unstable mode emerges and can be characterized — growth rate, frequency, structure.

The overall procedure is illustrated on three unstable modes arising in different base states through three different instability mechanisms. Long-wave mode as well as short-wave elliptic and curvature modes emerging through a subtle two-wave resonance phenomenon involving the base flow have been accurately described. Special attention has been paid to convergence with respect to the grid definition, as short-wave modes have radial length scales much smaller than the helix radius or pitch, here in a ratio of 1 to 100 typically. Results are shown to agree very closely with those derived from a standard fully three-dimensional procedure, which validates the new

procedure. With respect to the three-dimensional procedure, CPU time is divided by a factor roughly equal to the number of grid points that would be needed along the axial direction: computations are thus 100–1000 times faster. This feature makes parametric studies possible, e.g. branch continuation with respect to the axial wavenumber  $k_z$ , to Reynolds number, etc. It should be emphasized that here, the instability wavenumber  $k_z$  can be chosen arbitrarily, whereas in three-dimensional periodic formulations, it is quantized. For shortwave modes stemming from resonances and often characterized by very narrow instability tongues, this is a serious advantage. This numerical procedure makes the investigation of instabilities in helical vortex systems possible, and should improve the knowledge on the mechanisms at play in the transition of rotor wakes to turbulence.

However, owing to the assumptions needed to reduce the problem to a two-dimensional one, the procedure may suffer from some limitations, which are now discussed. First, the assumption of helical symmetry, which is often correct locally, clearly does not hold when considering the whole rotor wake. The helical radius is known to increase in the streamwise direction as the axial velocity gradually decreases, on typical distances comparable to the rotor diameter. In the meantime, the vortex-core radius evolves through viscous or turbulent diffusion, and so does the internal jet/wake component. The development of a long-wave instability may also change the spacing between successive coils, locally altering the pitch and the vortex-core deformation. Under such circumstances, the present study determines *local* instability properties at each downstream location. Second, section 3 describes a methodology to reach a fully developed base flow, i.e. a quasi-steady state of the Navier–Stokes equations, for which velocity and vorticity distributions in the vortex core are near Gaussian. The instability study of section 4 has been performed on such states. Yet, in practical situations, vorticity shed from the blades may roll up around the tip vortices [28], approaching steady solutions of Euler equations which are not Gaussian. The present procedure is able to compute the instability properties in this case as well: it is not limited to Gaussian states. Last, in the present study, flows are laminar, a strong limitation when considering engineering flows such as wind turbines. However, the present approach does not preclude the use of a turbulence model. Some studies couple the use of a turbulent base flow and the determination of instabilities [29, 30]: this is a priori valid when spatial scales are well separated. The turbulence model should then be adapted to helically symmetric flows, which, to our knowledge, is still to be done.

**Acknowledgements.** This work was supported by Collaborative Research Project 2022–2024, Institute of Fluid Science, Tohoku University. YH was supported by JSPS KAKENHI 21H01242. The three-dimensional numerical calculations were performed on AFI-NITY at the Institute of Fluid Science, Tohoku University.

## Appendix A Boundary condition at $r = R_{\text{ext}}$ for the HELIX code

Away from the vortex, the flow is potential. For all modes  $n \neq 0$ , we thus impose

$$\omega_B^{(n)} = u_H^{(n)} = 0. \quad (\text{A1})$$

The boundary condition on  $\Psi^{(n)}$  is imposed through a Robin condition (mixed boundary condition) at  $r = R_{\text{ext}}$ :

$$\partial_r[\Psi^{(n)}] = -|n|C_n\Psi^{(n)}(R_{\text{ext}}). \quad (\text{A2})$$

When  $L$  is infinite, the mode  $\Psi^{(n)}$  for the streamfunction satisfies away from the vortex

$$\frac{1}{r}\partial_r[r\partial_r(\hat{\Psi}^{(n)})] - \frac{n^2}{r^2}\hat{\Psi}^{(n)} = 0, \quad (\text{A3})$$

with solution  $\Psi^{(n)} = -iB/r^{|n|}$ , hence  $C_n = 1/R_{\text{ext}}$ . When  $L$  is finite, the procedure is different. In the potential region, the velocity field can also be expressed as the gradient of a solution  $\Phi$  of the Laplace equation. Mode  $\Phi^{(n)}$  then satisfies a modified Bessel equation. Using the decreasing solution at  $r \rightarrow \infty$ , this imposes

$$\Phi^{(n)} = BK_{|n|}(|\beta|r) \quad \text{with} \quad \beta = -\frac{n}{L}, \quad (\text{A4})$$

where  $K_{|n|}(\hat{r})$  is a modified Bessel function of the second kind [25]. Since, for all  $n \neq 0$

$$u_r^{(n)} = \frac{\partial\Phi^{(n)}}{\partial r} = \frac{in}{r}\Psi^{(n)}, \quad u_\varphi^{(n)} = \frac{in}{r\alpha}\Phi^{(n)} = -\alpha\frac{\partial\Psi^{(n)}}{\partial r}, \quad (\text{A5})$$

equations (A4) and (A5) yield

$$C_n = \frac{-L}{R_{\text{ext}}\alpha_{\text{ext}}^2} \frac{1}{H_{|n|}(\hat{R}_{\text{ext}})}, \quad (\text{A6})$$

where

$$\alpha_{\text{ext}}^2 \equiv \frac{1}{1 + R_{\text{ext}}^2/L^2}, \quad H_{|n|}(\hat{r}) \equiv \frac{K'_{|n|}(\hat{r})}{K_{|n|}(\hat{r})}, \quad \hat{r} \equiv |\beta|r, \quad \hat{R}_{\text{ext}} \equiv |\beta|R_{\text{ext}}. \quad (\text{A7})$$

For mode  $n = 0$ , since the flow is potential away from the vortex, we impose

$$\omega_B^{(0)} = u_H^{(0)} = 0. \quad (\text{A8})$$

For the velocity  $u_\varphi^{(0)}$ , equation (16) reads away from the vortex:

$$\partial_r \left[ r \alpha u_\varphi^{(0)} \right] = -2 \frac{r \alpha^4}{L} C_\infty \quad \text{with} \quad C_\infty = \frac{\Gamma}{2\pi L} + U_z^\infty. \quad (\text{A9})$$

This equation can be exactly integrated with the following condition at  $r = \infty$ :  $u_\varphi^{(0)}(\infty) = -U_z^\infty/L$ , which yields in the potential region

$$u_\varphi^{(0)} = -U_z^\infty \sqrt{\frac{1+x}{x}} + \frac{C_\infty}{\sqrt{x(x+1)}}, \quad x = (r/L)^2. \quad (\text{A10})$$

This Dirichlet condition is imposed at  $r = R_{\text{ext}}$ .

## Appendix B Function $H_{|n|}(\hat{r})$

Let us evaluate the function  $H_{|n|}(\hat{r})$  defined in equation (A7) which is based on a modified Bessel function of the second kind  $K_{|n|}(\hat{r})$  [25]. Let us introduce the small parameter  $\epsilon$  and the integer  $n_{\text{large}}$  e.g.  $\epsilon = 0.01$  and  $n_{\text{large}} = 10$ .

### B.1 Expressions for $H_0(\hat{r})$

Three cases can be distinguished:

- for small  $\hat{r} \leq \epsilon$ , the asymptotic form of the Bessel function  $K_0$  reads:

$$K_0(\hat{r}) \sim -\log\left(\frac{\hat{r}}{2}\right) - \gamma_c$$

involving the Euler–Mascheroni constant  $\gamma_c \approx 0.58$ , so that the function  $H_0$  behaves as:

$$H_0(\hat{r}) = \frac{K_0'(\hat{r})}{K_0(\hat{r})} \sim \frac{1}{\hat{r}(\gamma_c + \log(\frac{\hat{r}}{2}))}; \quad (\text{B11})$$

- for  $\epsilon < \hat{r} < 1/\epsilon$ , one uses a standard library to compute

$$H_0(\hat{r}) = \frac{K_0'(\hat{r})}{K_0(\hat{r})};$$

- for large  $\hat{r} \geq \frac{1}{\epsilon}$ , we use an asymptotic expression for the Bessel  $K_0$  function [25]

$$K_0(\hat{r}) \sim e^{-\hat{r}} \sqrt{\frac{\pi}{2\hat{r}}} \left( 1 - \frac{1}{8\hat{r}} + \text{O}(\hat{r}^{-2}) \right),$$

leading to the following expression:

$$H_0(\hat{r}) = \frac{K_0'(\hat{r})}{K_0(\hat{r})} \sim -\left( 1 + \frac{1}{2\hat{r}} \right). \quad (\text{B12})$$

## B.2 Expressions for $H_{|n|}(\hat{r})$ for $0 < |n| \leq n_{\text{large}}$

For  $|n| > 0$  the function  $H_{|n|}$  is such that

$$H_{|n|}(\hat{r}) \equiv \frac{1}{K_{|n|}(\hat{r})} \frac{\partial K_{|n|}(\hat{r})}{\partial \hat{r}} = -\frac{K_{|n|-1}}{K_{|n|}} - \frac{|n|}{\hat{r}}. \quad (\text{B13})$$

Three cases are distinguished:

- for small  $\hat{r} < \epsilon$ , since

$$H_1(\hat{r}) = \frac{K_1'(\hat{r})}{K_1(\hat{r})} \sim -\frac{1}{\hat{r}} \quad \text{for } |n| = 1,$$

one has

$$\frac{K_{|n|-1}(\hat{r})}{K_{|n|}(\hat{r})} \simeq \frac{\hat{r}}{|n|-1} \quad \text{if } |n| \geq 2,$$

so that

$$H_{|n|}(\hat{r}) \sim -\frac{|n|}{\hat{r}}; \quad (\text{B14})$$

- for  $\epsilon \leq \hat{r} \leq n_{\text{large}}^2$ , after using a standard library to compute the ratio of Bessel functions of the second kind  $K_0(\hat{r})/K_1(\hat{r})$ , one computes  $K_{|n|-1}(\hat{r})/K_{|n|}(\hat{r})$  using the recurrence:

$$\frac{K_{|n|}(\hat{r})}{K_{|n|+1}(\hat{r})} = \left[ \frac{K_{|n|-1}(\hat{r})}{K_{|n|}(\hat{r})} + \frac{2|n|}{\hat{r}} \right]^{-1}; \quad (\text{B15})$$

- for large  $\hat{r} > n_{\text{large}}^2$ , an asymptotic expression can be used for the Bessel  $K_{|n|}$  function [25]

$$K_{|n|}(\hat{r}) \sim e^{-\hat{r}} \sqrt{\frac{\pi}{2\hat{r}}} \left( 1 + \frac{4n^2 - 1}{8} \frac{1}{\hat{r}} + \mathcal{O}(\hat{r}^{-2}) \right),$$

and  $H_{|n|}(\hat{r})$  is thus expressed as:

$$H_{|n|}(\hat{r}) = \frac{K_{|n|}'(\hat{r})}{K_{|n|}(\hat{r})} \sim -\left( 1 + \frac{1}{2\hat{r}} \right). \quad (\text{B16})$$

## B.3 Expressions for $H_{|n|}(\hat{r})$ for $|n| > n_{\text{large}}$

Four cases can be distinguished:

- for  $\hat{r} < \epsilon|n|$ , as the asymptotic form of the Bessel function  $K_{|n|}$  reads:

$$K_{|n|}(\hat{r}) \propto \frac{1}{2} (|n|-1)! \left( \frac{\hat{r}}{2} \right)^{-|n|},$$

one has

$$\frac{K_{|n|-1}(\hat{r})}{K_{|n|}(\hat{r})} \simeq \frac{\hat{r}}{|n|-1},$$

and the function  $H_{|n|}$  thus behaves as:

$$H_{|n|}(\hat{r}) \propto -\frac{|n|}{\hat{r}}; \quad (\text{B17})$$

- for  $\epsilon|n| < \hat{r} < |n|/\epsilon$ , the following holds

$$H_{|n|}(\hat{r}) = \frac{K'_{|n|}(\hat{r})}{K_{|n|}(\hat{r})} = -\frac{|n|\sqrt{1 + \frac{\hat{r}^2}{|n|^2}}}{\hat{r}} \frac{|n| - V}{|n| - U}, \quad (\text{B18})$$

with

$$V \equiv \frac{1}{24}(-9p + 7p^3), \quad U \equiv \frac{1}{24}(3p - 5p^3), \quad p \equiv \frac{1}{\sqrt{1 + \frac{\hat{r}^2}{|n|^2}}};$$

- the case  $|n|/\epsilon < \hat{r} < |n|^2$  is never met in our computations;
- for  $|n|^2 \leq \hat{r}$ , an asymptotic expression can be used for the Bessel  $K_{|n|}$  function [25]

$$K_{|n|}(\hat{r})|_{\hat{r} \rightarrow +\infty} \propto e^{-\hat{r}} \sqrt{\frac{\pi}{2\hat{r}}} \left( 1 + \frac{4n^2 - 1}{8} \frac{1}{\hat{r}} + O(\hat{r}^{-2}) \right).$$

As a consequence,  $H_{|n|}(\hat{r})$  is expressed as:

$$H_{|n|}(\hat{r}) = \frac{K'_{|n|}(\hat{r})}{K_{|n|}(\hat{r})} \propto -\left( 1 + \frac{1}{2\hat{r}} \right). \quad (\text{B19})$$

## Appendix C Relating $\Pi_{\perp}$ and $\Pi_0$ planes

It is explained here how to transfer the data from plane  $\Pi_{\perp}$  to plane  $\Pi_0$  (see figure 2) in the HELIX and HELIKZ-LIN solvers. Indeed, this is useful to building the initial condition as well as characterizing the final state or instability modes. Starting from (27) and  $\overrightarrow{AM_{\perp}} = \rho \mathbf{e}_{\rho}$ , one gets

$$\overrightarrow{OM_{\perp}} = (r_A + \rho \cos \psi) \mathbf{e}_{\xi} + \rho \sin \psi \mathbf{e}_{\eta}. \quad (\text{C20})$$

If the point  $M_0 \in \Pi_0$  given by helical variables  $(r_{M_0}, \varphi_{M_0})$  belongs to the helical line passing through  $M_{\perp}$  (see figure 2b) then

$$\overrightarrow{OM_{\perp}} = L(\theta_{M_{\perp}} - \varphi_{M_0}) \mathbf{e}_z + r_{M_{\perp}} \mathbf{e}_r(\theta_{M_{\perp}}), \quad r_{M_{\perp}} = r_{M_0}. \quad (\text{C21})$$

Projecting the two equations (C20) and (C21) along the axis  $x$ ,  $y$  and  $z$ , gives

$$\begin{aligned} r_{M_0} \cos(\theta_{M_{\perp}}) &= (r_A + \rho \cos \psi) \cos \theta_A - \alpha_A \sin \theta_A \rho \sin \psi, \\ r_{M_0} \sin(\theta_{M_{\perp}}) &= (r_A + \rho \cos \psi) \sin \theta_A + \alpha_A \cos \theta_A \rho \sin \psi, \\ L(\theta_{M_{\perp}} - \theta_{M_0}) &= -\alpha_A \frac{r_A}{L} \rho \sin \psi. \end{aligned} \quad (\text{C22})$$

Knowing the values  $(\rho, \psi)$ , it is straightforward to determine  $r_{M_0}$  and the azimuthal location  $\theta_{M_\perp}$  from the first two equations of (C22) and to deduce the value of  $\theta_{M_0}$  through the last one. Now, using a standard procedure, it is easy to do the reverse and find  $(\rho, \psi)$  associated to a given location  $(r_0, \varphi_0)$  inside the vortex. Indeed, this is useful for the initial condition of the HELIX code: one computes the fields  $\omega_B(r_0, \varphi_0)$  and  $u_H(r_0, \varphi_0)$  at specific points  $(r_0, \varphi_0)$ . Once this done, the symmetry (10) yields  $\omega_B(r_0, \theta_{M_0}) = \omega_B(\rho)$  and  $u_H(r_0, \theta_{M_0}) = u_H(\rho)$  directly from the analytic formula (28).

To now characterize the final state of a simulation in the  $\Pi_\perp$  plane, we need to express the velocity field at point  $M_\perp$  using the basis  $(\mathbf{e}_\rho, \mathbf{e}_\psi, \mathbf{e}_b)$

$$\mathbf{u}(M_\perp) = u_\rho(M_\perp)\mathbf{e}_\rho + u_\psi(M_\perp)\mathbf{e}_\psi + u_b(M_\perp)\mathbf{e}_b,$$

with respect to the velocity field at the corresponding point  $M_0$  in plane  $\Pi_0$  given by

$$\mathbf{u}(M_0) = u_r(M_0)\mathbf{e}_r(M_0) + u_\varphi(M_0)\mathbf{e}_\varphi(M_0) + u_B(M_0)\mathbf{e}_B(M_0).$$

The helical symmetry implies

$$\mathbf{u}(M_\perp) = u_r(M_0)\mathbf{e}_r(M_\perp) + u_\varphi(M_0)\mathbf{e}_\varphi(M_\perp) + u_B(M_0)\mathbf{e}_B(M_\perp).$$

Projected on the basis  $(\mathbf{e}_\rho, \mathbf{e}_\psi, \mathbf{e}_b)$ , this yields

$$\begin{pmatrix} u_\rho(M_\perp) \\ u_\psi(M_\perp) \\ u_b(M_\perp) \end{pmatrix} = [u_r(M_0)\mathbf{e}_r(M_\perp) + u_\varphi(M_0)\mathbf{e}_\varphi(M_\perp) + u_B(M_0)\mathbf{e}_B(M_\perp)] \cdot \begin{pmatrix} \cos \psi \mathbf{e}_\xi + \sin \psi \mathbf{e}_\eta \\ -\sin \psi \mathbf{e}_\xi + \cos \psi \mathbf{e}_\eta \\ \mathbf{e}_b \end{pmatrix},$$

where

$$\begin{aligned} \mathbf{e}_r(M_\perp) \cdot \mathbf{e}_\xi &= \cos(\theta_{M_\perp} - \theta_A), \\ \mathbf{e}_r(M_\perp) \cdot \mathbf{e}_\eta &= \alpha_A \sin(\theta_{M_\perp} - \theta_A), \\ \mathbf{e}_r(M_\perp) \cdot \mathbf{e}_b &= \alpha_A \frac{r_A}{L} \sin(\theta_{M_\perp} - \theta_A), \\ \mathbf{e}_\varphi(M_\perp) \cdot \mathbf{e}_\xi &= \alpha_{M_\perp} \sin(\theta_A - \theta_{M_\perp}), \\ \mathbf{e}_\varphi(M_\perp) \cdot \mathbf{e}_\eta &= \alpha_{M_\perp} \alpha_A \left[ \frac{r_{M_\perp} r_A}{L^2} + \cos(\theta_{M_\perp} - \theta_A) \right], \\ \mathbf{e}_\varphi(M_\perp) \cdot \mathbf{e}_b &= \alpha_{M_\perp} \alpha_A \left[ -\frac{r_{M_\perp}}{L} + \frac{r_A}{L} \cos(\theta_{M_\perp} - \theta_A) \right], \\ \mathbf{e}_B(M_\perp) \cdot \mathbf{e}_\xi &= \alpha_{M_\perp} \frac{r_{M_\perp}}{L} \sin(\theta_A - \theta_{M_\perp}), \\ \mathbf{e}_B(M_\perp) \cdot \mathbf{e}_\eta &= \alpha_{M_\perp} \alpha_A \left[ -\frac{r_A}{L} + \frac{r_{M_\perp}}{L} \cos(\theta_{M_\perp} - \theta_A) \right], \\ \mathbf{e}_B(M_\perp) \cdot \mathbf{e}_b &= \alpha_{M_\perp} \alpha_A \left[ 1 + \frac{r_{M_\perp} r_A}{L^2} \cos(\theta_{M_\perp} - \theta_A) \right]. \end{aligned}$$

To express the vorticity field located at  $M_\perp$  using the basis  $(\mathbf{e}_\rho, \mathbf{e}_\psi, \mathbf{e}_b)$

$$\boldsymbol{\omega}(M_\perp) = \omega_\rho(M_\perp)\mathbf{e}_\rho + \omega_\psi(M_\perp)\mathbf{e}_\psi + \omega_b(M_\perp)\mathbf{e}_b$$

with respect to the vorticity field at the corresponding point  $M_0$  in plane  $\Pi_0$ , the same procedure applies and provides expressions connecting the vorticity field located at  $M_\perp$  and  $M_0$ .

Let us emphasize that velocity and vorticity components  $u_b(M_\perp)$  and  $\omega_b(M_\perp)$  differ from components  $u_B(M_\perp)$  and  $\omega_B(M_\perp)$  except when  $M_\perp = A$ .

## Appendix D Numerical treatment of solver HELIKZ-LIN for stability modes

In the code HELIKZ-LIN, equations as well as boundary conditions are discretized using staggered grids in the  $(r, \varphi)$  plane (see figure D1). Radial differentiations use 2nd order schemes that are centered at interior points. Differentiations in  $\varphi$  are performed in the spectral space. Time advance is also performed in the spectral space in two steps: (i) a prediction step using progressive 2nd order finite differences in time, where viscous VT terms (58) are fully implicit while LNL terms (61) are evaluated using a 2nd order Adams–Bashforth extrapolation scheme; (ii) a projection step that evaluates the pressure that allows to update the velocity field to meet the incompressibility condition.

The outer boundary is set at the finite radius  $r = R_{\text{ext}}$  that is located in away from the vorticity region. The mesh used in plane  $\Pi_0$  is regular in both radial and azimuthal direction, with  $N_r = 768$  or  $1024$  grid points along the radial direction. In the azimuthal direction, we select  $N_\theta = \frac{3}{2} \times 256$  grid points but, because of the standard 2/3 antialiasing procedure, only azimuthal modes  $-128 < n \leq 128$  are effectively used.

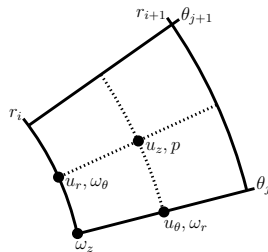


Fig. D1 HELIKZ solver: elementary cell showing where the quantities are located.

### D.1 Boundary conditions at the outer boundary $r = R_{\text{ext}}$

To determine the boundary conditions at  $r = R_{\text{ext}}$ , we use the condition (62) obtained by assuming that the flow is potential at this outer boundary. Boundary conditions

to be imposed at  $r = R_{\text{ext}}$  are Robin conditions (mixed boundary conditions)

$$\frac{\partial \Phi^{(n)}}{\partial r} = C_{\Phi}^{(n)} \Phi^{(n)} \quad (\text{D23})$$

$$\frac{\partial v_r^{(n)}}{\partial r} = C_r^{(n)} v_r^{(n)}, \quad \frac{\partial v_{\theta}^{(n)}}{\partial r} = C_{\theta}^{(n)} v_{\theta}^{(n)}, \quad \frac{\partial v_z^{(n)}}{\partial r} = C_z^{(n)} v_z^{(n)}, \quad (\text{D24})$$

where  $C_{\Phi}^{(n)}$ ,  $C_r^{(n)}$ ,  $C_{\theta}^{(n)}$  and  $C_z^{(n)}$  are constants listed below (proofs involve very standard calculations).

We set

$$\hat{r} \equiv |\beta|r, \quad \hat{R}_{\text{ext}} = |\beta|R_{\text{ext}}, \quad \beta \equiv k_z - \frac{n}{L}. \quad (\text{D25})$$

When  $k_z \neq n/L$ , we have

$$C_{\Phi}^{(n)} = C_z^{(n)} = |\beta|H_{|n|}(\hat{R}_{\text{ext}}), \quad C_r^{(n)} = \frac{\beta^2 + n^2/R_{\text{ext}}^2}{C_{\Phi}^{(n)}} - \frac{1}{R_{\text{ext}}}, \quad C_{\theta}^{(n)} = C_{\Phi}^{(n)} - \frac{1}{R_{\text{ext}}}, \quad (\text{D26})$$

where expressions for  $H_{|n|}$  are given in Appendix B.

When  $k_z = n/L$ , the conditions become

$$C_{\Phi}^{(n)} = -\frac{|n|}{R_{\text{ext}}}, \quad C_r^{(n)} = C_{\theta}^{(n)} = -\frac{|n|+1}{R_{\text{ext}}}, \quad u_x^{(n)} = 0. \quad (\text{D27})$$

## D.2 Randomized initial condition

Given an axial wavelength  $k_z$ , we run the solver HELIKZ-LIN with an initial condition for the complex velocity perturbations. It generally consists of colored noise set only in the region of nonzero basic vorticity. First we generate real and imaginary parts of radial, azimuthal and axial components in the Fourier space

$$\hat{f}_{\alpha}^{(n)}(r_i) = \exp \left[ -\left( \frac{r_i - r_0}{\Delta r} \right)^6 \right] \exp \left[ -\left( \frac{n - n_0}{\Delta n} \right)^4 \right] \xi_i^{(n)}, \quad \alpha = r, \theta, z, \quad (\text{D28})$$

where  $\xi_i^{(n)}$  are random fields uniform in  $[-\frac{1}{2}, \frac{1}{2}]$ . The multiplicative factors limit the radial range of the perturbations and its spectral extent ( $r_0 = 1$ ,  $\Delta r = 0.3$ ,  $n_0 = 42$  and  $\Delta n = 42$ ). The filter in  $r$  is introduced to avoid the singular polar axis. Second these fields are transformed to the physical space. In order to restrict the perturbation to the region of non vanishing basic vorticity, we filter the perturbation according to  $\tilde{v}_{\alpha}(r_i, \theta_j) = M(r_i, \theta_j) \hat{f}_{\alpha}(r_i, \theta_j)$  where the value of the mask  $M$  depends on the level of the normalized basic vorticity  $\omega^{\text{BF}}/\max(\omega^{\text{BF}})$  at point  $(r_i, \theta_j)$ <sup>1</sup>. Third, the components are transformed back to spectral space where a projection is performed to get a divergenceless velocity field  $\hat{\mathbf{u}}$ . The resulting field is then normalized so that the maximum modulus over the values of the 3 velocity components is  $10^{-2}$ . Figure D2

<sup>1</sup>Specifically, if  $\omega^{\text{BF}}/\max(\omega^{\text{BF}}) < 10^{-2}$ , then  $M = 0$ , if  $\omega^{\text{BF}}/\max(\omega^{\text{BF}}) > 10^{-1}$ , then  $M = 1$ , while  $M$  takes intermediate values between these two thresholds (a cubic spline is used in between).

presents an example of initial condition in the  $\Pi_0$  plane with  $R_{\text{ext}} = 2$ ,  $N_r = 768$  and  $N_\theta = 384$ .

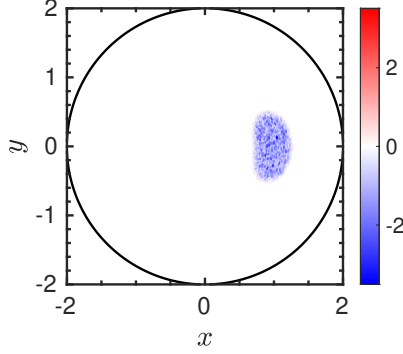


**Fig. D2** An example of initial perturbation with  $k_z = 20$  displayed in the  $\Pi_0$  plane: the real part of axial vorticity  $\omega'_z$  for the base state BS3 ( $L = 0.7$ ,  $a = 0.15$ ,  $W_0 = 0.2$ ).

There are two cases where the initial condition does not consist in the above noise distribution. The first instance corresponds to branch continuation, where we gradually change the parameter  $k_z$ : the code is restarted from the final state of another run. For instance, the state at  $t = 150$  for  $k_z = 20$  represented in figure 6c can be used as initial condition for a simulation at  $k_z = 19.9$  or at  $k_z = 20.1$ . Then convergence can be reached after a time period as short as  $t = 10$ , but this naturally depends on the step in  $k_z$  selected and might substantially vary along the branch. The second instance corresponds to changes of mesh resolution. In this case, both base flow and complex mode are interpolated/extrapolated on a different grid, before the code is restarted. This has been extensively used in the convergence study presented in §6.1.

## Appendix E Numerical treatment of three-dimensional linearized Navier–Stokes equations

### E.1 Temporal discretization

We write the linearized incompressible Navier–Stokes equations in the following form

$$\begin{aligned} \frac{\partial u'_r}{\partial t} &= H_u + \nu \left( \nabla^2 - \frac{1}{r^2} \right) u'_r - \nu \frac{2}{r^2} \frac{\partial u'_\theta}{\partial \theta}, \\ \frac{\partial u'_\theta}{\partial t} &= H_v + \nu \left( \nabla^2 - \frac{1}{r^2} \right) u'_\theta + \nu \frac{2}{r^2} \frac{\partial u'_r}{\partial \theta}, \\ \frac{\partial u'_z}{\partial t} &= H_w + \nu \nabla^2 u'_z, \end{aligned} \tag{E29}$$

$$0 = \frac{\partial u'_r}{\partial r} + \frac{u'_r}{r} + \frac{1}{r} \frac{\partial u'_\theta}{\partial \theta} + \frac{\partial u'_z}{\partial z}, \tag{E30}$$

where

$$\nabla^2 = \frac{\partial^2}{\partial r^2} + \frac{1}{r} \frac{\partial}{\partial r} + \frac{1}{r^2} \frac{\partial^2}{\partial \theta^2} + \frac{\partial^2}{\partial z^2}$$

and

$$H_u = h_u - \frac{\partial p'}{\partial r}, \quad H_v = h_v - \frac{1}{r} \frac{\partial p'}{\partial \theta}, \quad H_w = h_w - \frac{\partial p'}{\partial z}, \quad (\text{E31})$$

with

$$\begin{aligned} h_u &= -u_r^{\text{BF(T)}} \frac{\partial u_r'}{\partial r} - \frac{u_\theta^{\text{BF(T)}}}{r} \frac{\partial u_r'}{\partial \theta} - u_z^{\text{BF(T)}} \frac{\partial u_r'}{\partial z} + \frac{2u_\theta^{\text{BF(T)}} u_\theta'}{r} \\ &\quad - u_r' \frac{\partial u_r^{\text{BF(T)}}}{\partial r} - u_\theta' \frac{\partial u_r^{\text{BF(T)}}}{\partial \theta} - u_z' \frac{\partial u_r^{\text{BF(T)}}}{\partial z}, \\ h_v &= -u_r^{\text{BF(T)}} \frac{\partial u_\theta'}{\partial r} - \frac{u_\theta^{\text{BF(T)}}}{r} \frac{\partial u_\theta'}{\partial \theta} - u_z^{\text{BF(T)}} \frac{\partial u_\theta'}{\partial z} - \frac{u_\theta^{\text{BF(T)}} u_r'}{r} - \frac{u_r^{\text{BF(T)}} u_\theta'}{r} \\ &\quad - u_r' \frac{\partial u_\theta^{\text{BF(T)}}}{\partial r} - u_\theta' \frac{\partial u_\theta^{\text{BF(T)}}}{\partial \theta} - u_z' \frac{\partial u_\theta^{\text{BF(T)}}}{\partial z}, \\ h_w &= -u_r^{\text{BF(T)}} \frac{\partial u_z'}{\partial r} - \frac{u_\theta^{\text{BF(T)}}}{r} \frac{\partial u_z'}{\partial \theta} - u_z^{\text{BF(T)}} \frac{\partial u_z'}{\partial z} \\ &\quad - u_r' \frac{\partial u_z^{\text{BF(T)}}}{\partial r} - u_\theta' \frac{\partial u_z^{\text{BF(T)}}}{\partial \theta} - u_z' \frac{\partial u_z^{\text{BF(T)}}}{\partial z}. \end{aligned} \quad (\text{E32})$$

The velocity fields are expanded in Fourier series as

$$u_r' = \sum_{n,q} \hat{u}_{n,q}(r,t) e^{i(n\theta + qk_0 z)} \quad (\text{E33})$$

with similar expansions for  $u_\theta'$  and  $u_z'$ , where  $k_0 = 2\pi/L_{\text{box}}$ . In temporal discretization with the Crank–Nicolson scheme for the viscous terms, the cross terms  $2\nu r^{-2} \partial u_\theta' / \partial \theta$  and  $2\nu r^{-2} \partial u_r' / \partial \theta$  in (E29) are moved to  $H_u$  and  $H_v$  together with the corresponding terms taking account of the behaviour of  $\hat{u}_{n,q}$  and  $\hat{v}_{n,q}$  near  $r = 0$

$$\begin{aligned} \hat{u}_{n,q} &= Ar^{|n|-1} + \text{O}(r^{|n|}), \quad \hat{v}_{n,q} = i \operatorname{sgn}(n) Ar^{|n|-1} + \text{O}(r^{|n|}) \quad \text{for } n \neq 0, \\ \hat{u}_{0,q} &= Ar + \text{O}(r^2), \quad \hat{v}_{0,q} = Br + \text{O}(r^2). \end{aligned} \quad (\text{E34})$$

This makes the numerical procedure simpler. The resulting discretized equations in the Fourier space are

$$\begin{aligned} \left[ 1 - \nu \frac{\Delta t}{2} D_{|n|-1,q} \right] \hat{u}_{n,q}^{(l+1)} &= \frac{\Delta t}{2} \left( 3\hat{H}_{u;n,q}^{(l)} - \hat{H}_{u;n,q}^{(l-1)} \right) + \left[ 1 + \nu \frac{\Delta t}{2} D_{|n|-1,q} \right] \hat{u}_{n,q}^{(l)} \\ \left[ 1 - \nu \frac{\Delta t}{2} D_{|n|-1,q} \right] \hat{v}_{n,q}^{(l+1)} &= \frac{\Delta t}{2} \left( 3\hat{H}_{v;n,q}^{(l)} - \hat{H}_{v;n,q}^{(l-1)} \right) + \left[ 1 + \nu \frac{\Delta t}{2} D_{|n|-1,q} \right] \hat{v}_{n,q}^{(l)} \\ \left[ 1 - \nu \frac{\Delta t}{2} D_{n,q} \right] \hat{w}_{n,q}^{(l+1)} &= \frac{\Delta t}{2} \left( 3\hat{H}_{w;n,q}^{(l)} - \hat{H}_{w;n,q}^{(l-1)} \right) + \left[ 1 + \nu \frac{\Delta t}{2} D_{n,q} \right] \hat{w}_{n,q}^{(l)}, \end{aligned} \quad (\text{E35})$$

where  $f^{(l)}$  denotes the value of  $f$  at the  $l$ -th time step and

$$D_{n,q} \equiv \frac{d^2}{dr^2} + \frac{1}{r} \frac{d}{dr} - \left( \frac{n^2}{r^2} + k_0^2 q^2 \right), \quad (\text{E36})$$

$$\begin{aligned} \hat{H}_{u;n,q} &\equiv \hat{h}_{u;n,q} - \frac{\partial \hat{p}_{n,q}}{\partial r} + \frac{2\nu}{r^2} (-|n|\hat{u}_{n,q} - in\hat{v}_{n,q}), \\ \hat{H}_{v;n,q} &\equiv \hat{h}_{v;n,q} - in\frac{\hat{p}_{n,q}}{r} + \frac{2\nu}{r^2} (-|n|\hat{v}_{n,q} + in\hat{u}_{n,q}), \\ \hat{H}_{w;n,q} &\equiv \hat{h}_{w;n,q} - ik_0q\hat{p}_{n,q}. \end{aligned} \quad (\text{E37})$$

The boundary conditions (74) at  $r = R_{\text{far}}$  become

$$\hat{u}_{n,q} = 0, \quad \frac{\partial}{\partial r}(r\hat{v}_{n,q}) = \frac{\partial \hat{w}_{n,q}}{\partial r} = 0.$$

The Poisson equation for  $p'$  is also expressed in the Fourier space as

$$\left[ \frac{d^2}{dr^2} + \frac{1}{r} \frac{d}{dr} - \left( \frac{n^2}{r^2} + k_0^2 q^2 \right) \right] \hat{p}_{n,q} = \frac{d\hat{h}_{u;n,q}}{dr} + \frac{\hat{h}_{u;n,q}}{r} + \frac{im}{r} \hat{h}_{v;n,q} + ik_0q\hat{h}_{w;n,q}, \quad (\text{E38})$$

with the boundary condition

$$\frac{\partial \hat{p}_{n,q}}{\partial r} = 0.$$

The equations (E35) and (E38) for each Fourier mode are second-order ordinary differential equations; they are solved by a sixth-order accurate compact scheme.

## E.2 Randomized initial condition

The initial condition is made up with a randomized field localized in the region of the basic vorticity, and furthermore, has the spatial dependency expected for instability modes, as explained below.

First, a randomized scalar field is generated: for each component of the velocity field in the cylindrical coordinate system, a one-dimensional scalar field  $f_\alpha$  in  $\theta$  is generated in the Fourier space as

$$\hat{f}_\alpha^{(n)} = \xi_1 \exp(2\pi i \xi_2) \exp \left[ - \left( \frac{n}{\Delta n} \right)^2 \right], \quad \alpha = r, \theta, z, \quad (\text{E39})$$

where  $\xi_1$  and  $\xi_2$  are random numbers uniform in  $[0, 1]$  and  $\Delta n \equiv 2pL/R$  (integer  $p$  is the number of instability wavelengths within the numerical domain). Then, the field

is made local in two dimensions: a two-dimensional field is created from  $f_\alpha$  as

$$g_\alpha(r, \theta) = \exp \left[ - \left( \frac{r - r_0}{\Delta r} \right)^2 \right] \exp \left[ - \left( \frac{\theta - \theta_0}{\Delta \theta} \right)^2 \right] f_\alpha(\theta), \quad (\text{E40})$$

where  $\Delta r = 0.2R$ ,  $\Delta \theta = \Delta r/L$  and  $(r_0, \theta_0)$  is the position of the base helical vortex.

A three-dimensional field is then created as follows. In the periodic box of axial extent  $2\pi n_p L$ , three-dimensional components can be represented as combinations of modes  $(n, q)$  of the form  $\hat{v}_\alpha^{(n, q)}(r) \exp[in\theta + iqz/(n_p L)] + \text{c.c.}$  On the other hand, the instability modes of the helical vortex system are expected to be of the form  $A(r) \exp(in\varphi + ik_z z)$  or, since  $\varphi \equiv \theta - z/L$ ,

$$A(r) \exp \left[ in\theta + i(p - n_p n) \frac{z}{n_p L} \right].$$

The two-dimensional field  $\mathbf{g}$  can thus be transformed to a three-dimensional field of the above form by setting

$$\hat{v}_\alpha^{(n, q)}(r) = \hat{g}_\alpha^{(n)}(r) \delta_{qq_0}, \quad q_0 \equiv p - n_p n, \quad (\text{E41})$$

where  $\delta_{ij}$  stands for the Kronecker symbol. The Fourier coefficients are then forced to satisfy

$$\hat{v}_\alpha^{(-n, -q)}(r) = \hat{v}_\alpha^{(n, q)}(r)^\dagger \quad (\text{E42})$$

so that the field  $\mathbf{v} = v_r \mathbf{e}_r + v_\theta \mathbf{e}_\theta + v_z \mathbf{e}_z$  be indeed real. Finally,  $\mathbf{v}$  is projected to yield the divergenceless field  $\mathbf{u}$ :

$$\mathbf{u} = \mathbf{v} - \nabla \Phi, \quad \nabla^2 \Phi = \nabla \cdot \mathbf{v}. \quad (\text{E43})$$

## References

- [1] Le Dizès, S., Lacaze, L.: An asymptotic description of vortex Kelvin modes. *J. Fluid Mech.* **542**, 69–96 (2005)
- [2] Lessen, M., Singh, P.J., Paillet, F.: The stability of a trailing line vortex. Part 1. Inviscid theory. *J. Fluid Mech.* **63**, 753–763 (1974)
- [3] Mayer, E.W., Powell, K.G.: Viscous and inviscid instabilities of a trailing vortex. *J. Fluid Mech.* **245**, 91–114 (1992)
- [4] Porté-Agel, F., Bastankhah, M., Shamsoddin, S.: Wind-turbine and wind-farm flows: a review. *Boundary-Layer Meteorology* **174**(1), 1–59 (2020)

- [5] Hattori, Y., Fukumoto, Y.: Modal stability analysis of a helical vortex tube with axial flow. *J. Fluid Mech.* **738**, 222–249 (2014) <https://doi.org/10.1017/jfm.2013.591>
- [6] Blanco-Rodríguez, F.J., Le Dizès, S.: Elliptic instability of a curved batchelor vortex. *J. Fluid Mech.* **804**, 224–247 (2016) <https://doi.org/10.1017/jfm.2016.533>
- [7] Blanco-Rodríguez, F.J., Le Dizès, S.: Curvature instability of a curved batchelor vortex. *J. Fluid Mech.* **814**, 397–415 (2017) <https://doi.org/10.1017/jfm.2017.34>
- [8] Hattori, Y., Blanco-Rodríguez, F.J., Le Dizès, S.: Numerical stability analysis of a vortex ring with swirl. *J. Fluid Mech.* **878**, 5–36 (2019)
- [9] Widnall, S.E.: The stability of a helical vortex filament. *J. Fluid Mech.* **54**(4), 641–663 (1972)
- [10] Gupta, B., Loewy, R.: Theoretical analysis of the aerodynamic stability of multiple, interdigitated helical vortices. *AIAA journal* **12**(10), 1381–1387 (1974)
- [11] Okulov, V., Sørensen, J.N.: Stability of helical tip vortices in a rotor far wake. *Journal of Fluid Mechanics* **576**, 1–25 (2007)
- [12] Dahlberg, J., Alfredsson, P.: A preliminary wind tunnel study of windmill wake dispersion in various flow conditions. The Aeronautical Research Institute of Sweden, Bromma (1979)
- [13] Felli, M., Camussi, R., Di Felice, F.: Mechanisms of evolution of the propeller wake in the transition and far fields. *Journal of Fluid Mechanics* **682**, 5–53 (2011)
- [14] Quaranta, H.U., Bolnot, H., Leweke, T.: Long-wave instability of a helical vortex. *Journal of Fluid Mechanics* **780**, 687–716 (2015)
- [15] Leweke, T., Le Dizes, S., Williamson, C.H.: Dynamics and instabilities of vortex pairs. *Annual Review of Fluid Mechanics* **48**, 507–541 (2016)
- [16] Quaranta, H.U., Brynjell-Rahkola, M., Leweke, T., Henningson, D.S.: Local and global pairing instabilities of two interlaced helical vortices. *J. Fluid Mech.* **863**, 927–955 (2019) <https://doi.org/10.1017/jfm.2018.904>
- [17] Ivanell, S., Mikkelsen, R., Sørensen, J.N., Henningson, D.: Stability analysis of the tip vortices of a wind turbine. *Wind Energy* **13**(8), 705–715 (2010)
- [18] Abraham, A., Ramos-García, N., Sørensen, J.N., Leweke, T.: Numerical investigation of rotor asymmetry to promote wake recovery. *Journal of Physics: Conference Series* **2505**(1), 012032 (2023) <https://doi.org/10.1088/1742-6596/2505/1/012032>
- [19] Selçuk, C., Delbende, I., Rossi, M.: Helical vortices: Quasiequilibrium states and

- their time evolution. *Physical Review Fluids* **2**(8), 084701 (2017)
- [20] Wood, D., Boersma, J.: On the motion of multiple helical vortices. *J. Fluid Mech.* **447**, 149–171 (2001)
- [21] Brynjell-Rahkola, M., Henningson, D.S.: Numerical realization of helical vortices: application to vortex instability. *Theoret. Comput. Fluid Dynamics* **34**, 1–20 (2020) <https://doi.org/10.1007/s00162-019-00509-8>
- [22] Batchelor, G.K.: Axial flow in trailing line vortices. *J. Fluid Mech.* **20**, 645–658 (1964)
- [23] Xu, Y., Delbende, I., Rossi, M.: Quasi-equilibrium states for helical vortices with swirl. *J. Fluid Mech.* **944**, 24 (2022)
- [24] Delbende, I., Rossi, M., Daube, O.: DNS of flows with helical symmetry. *Theoret. Comput. Fluid Dynamics* **26**(1), 141–160 (2012) <https://doi.org/10.1007/s00162-011-0241-y>
- [25] Abramowitz, M., Stegun, I.A.: *Handbook of Mathematical Functions with Formulas, Graphs, and Mathematical Tables*, ninth dover printing, tenth gpo printing edn. *Mathematica*, New York (1964)
- [26] Lopez, J.M., Marques, F., Shen, J.: An efficient spectral-projection method for the navier–stokes equations in cylindrical geometries: Ii. three-dimensional cases. *J. Comput. Phys.* **176**(2), 384–401 (2002)
- [27] Lele, S.K.: Compact finite-difference schemes with spectral-like resolution. *J. Comput. Phys.* **103**, 16–42 (1992)
- [28] Schröder, D., Leweke, T., Hörnschemeyer, R., Stumpf, E.: Instability and merging of a helical vortex pair in the wake of a rotor. In: *Journal of Physics: Conference Series*, vol. 1934, p. 012007 (2021). IOP Publishing
- [29] Reynolds, W., Hussain, A.: The mechanics of an organized wave in turbulent shear flow. part 3. theoretical models and comparisons with experiments. *Journal of Fluid Mechanics* **54**(2), 263–288 (1972)
- [30] Viola, F., Iungo, G.V., Camarri, S., Porté-Agel, F., Gallaire, F.: Prediction of the hub vortex instability in a wind turbine wake: stability analysis with eddy-viscosity models calibrated on wind tunnel data. *J. Fluid Mech.* **750**, 1 (2014)